LATVIAN
JOURNAL
of
PHYSICS
and TECHNICAL
SCIENCES

ISSN 0868 - 8257

1

(Vol. 59)

2022

CONTENTS

LATVIAN
JOURNAL
of
PHYSICS
and TECHNICAL
SCIENCES

LATVIJAS
FIZIKAS
un TEHNISKO
ZINĀTŅU
ŽURNĀLS

ЛАТВИЙСКИЙ
ФИЗИКО-
ТЕХНИЧЕСКИЙ
ЖУРНАЛ

Published six times a year since February 1964
Iznāk sešas reizes gadā kopš 1964. gada februāra
Выходит шесть раз в год с февраля 1964 года

1 (Vol. 59) • 2022

RĪGA

Language Editor: O. Ivanova
Computer Designer: I. Begicevs

INDEXED (PUBLISHED) IN

www.scopus.com
www.sciendo.com
EBSCO (Academic Search Complete, www.epnet.com), INSPEC (www.iee.org.com).
VINITI (www.viniti.ru), Begell House Inc/ (EDC, www.edata-center.com).

Issuers: Institute of Physical Energetics,
Institute of Solid State Physics, University of Latvia
Registration Certificate Number: 000700221

Editorial Contacts:
11 Krivu Street, Riga, LV - 1006
Ph.: + 371 67551732
E-mail: leo@lza.lv
www.fei-web.lv

LATVIAN JOURNAL OF PHYSICS
AND TECHNICAL SCIENCES
2022, N 1

DOI: 10.2478/lpts-2022-0001

EVALUATION OF RECEIVED SIGNAL POWER LEVEL AND THROUGHPUT DEPENDING ON DISTANCE TO TRANSMITTER IN TESTBED FOR AUTOMOTIVE WLAN IEEE 802.11AC COMMUNICATION NETWORK

A. Ancans*, E. Petersons, R. Jerjomins,
E. Grabs, G. Ancans, A. Ipatovs

Institute of Telecommunications, Riga Technical University,
12 Azenes Str., Riga, LV-1048, LATVIA
*e-mail: arnis.ancans@gmail.com

WLAN IEEE 802.11ac is one of the wireless network technologies that can be used for ITS (Intelligent Transport Systems) needs, in particular for providing vehicle passengers with access to the data transmission network. To evaluate the performance of such automotive wireless access networks, it is necessary to perform experimental measurements. By conducting the throughput measurements in WLAN-based automotive communications testbed, it has been observed that the throughput of the communication channel decreases and the received signal becomes weaker as the vehicle moves away from the wireless access point. The aim of the research is to verify theoretically whether there is a correlation between the received signal power level and the throughput of the communication channel depending on the distance to the transmitter. To calculate the received signal power depending on the distance to the transmitter, a log-normal signal propagation model can be used, which takes into account random signal fluctuations that are described by the Nakagami distribution. Further, based on the obtained results, Shannon's theorem can be used to calculate the maximum theoretical throughput of the communication channel. The analysis of the obtained results shows that a correlation exists between the received signal power level and the throughput of the communication channel depending on the distance to the transmitter. The performed theoretical calculations justify the experimentally obtained results.

Keywords: *Experimental results, IEEE 802.11ac, received signal power level, theoretical Nakagami distribution, throughput.*

1. INTRODUCTION

The throughput is a measure of how much data traffic is successfully received at the intended destination per unit of time. The throughput achievable at different layers of the OSI (Open System Interconnection) model varies. In Section 4, the term "throughput" is applied either to communication channel maximum throughput, which is equivalent to the system capacity [1] and is measured at the physical layer [2], or the term is applied to the application layer throughput, which is called goodput, and is accordingly measured at the application layer [3]. In case the term "goodput" is used, the amount of data considered excludes protocol overhead bits and also retransmitted data packets [3]. In turn, when determining the capacity of a communication channel, the overheads introduced by higher layers are not considered. Often, the term "throughput" is also used in a general context without mentioning the specific OSI layer where it is measured, or it is applied to transport layer throughput. The term "throughput" is also used in a general context in this article.

In vehicular communication networks based on the WLAN (Wireless Local Area Network) IEEE 802.11, a movement speed of mobile client corresponds to a vehicle driving speed. The average individually achievable throughput of such mobile clients will be lower compared to the standard stationary or nomadic WLAN client. The difference in average performance to be achieved is mainly related to the different moving speeds of clients. As a vehicle speed increases, the mobile client is forced to perform more frequent handover procedures between wireless access points (APs). Consequently, the active data transmission time in AP coverage area decreases and proportionally more time is spent on the organisation and execution of the handover procedure [4]. Another important reason for the decrease in average throughput is the impact of environment on wireless data transmission, which becomes much more aggressive, compared to standard client movement conditions. At higher velocities, radio waves are reflected more intensively, and various and rapidly changing sources of external interference are possible. This increases a probability that client data may be lost or corrupted, which in turn means that the lost data will need to be retransmitted. As a result, application layer throughput (goodput) decreases as overheads increase [3]. This may also lead to an increase in the delay of handover procedure [4]. When assessing the theoretically possible throughput of a communication channel, it is important to consider both the distance between the mobile client and the transmitter, and the possible multipath propagation of signals. The theoretically obtained results can be compared with the experimentally obtained data; thus, the used mathematical models can be verified. The obtained results can also be used to improve the handover algorithms of the mobile client, where the fluctuations of the received signals would be considered.

This paper is organised as follows. Section 2 provides an overview of related works. In Section 3, we evaluate signal power level dependence on the distance to the transmitter with and without signal fluctuations. Section 4 provides the evaluation of throughput dependence on the power level of the received signal and the distance to the transmitter. Concluding remarks are presented in Section 5.

2. RELATED WORKS

In several studies, the power level of received signal *RSS* (Received Signal Strength) in the WLAN (also referred as WiFi) [5] is estimated depending on the distance to the transmitter. Estimates were performed both theoretically, for example, using two-ray flat-earth, free-space path loss or log-normal models [6], [7], and experimentally by performed *RSS* measurements [8], [9]. In practice, such multipath propagation causes fluctuations in the power of the received signal. This should be considered when assessing the WiFi network throughput theoretically, because these power fluctuations directly affect system performance, i.e., throughput. The study [10] proposes a model for estimating the capacity of several competing IEEE 802.11 systems based on radio wave propagation theory and the Shannon's theorem. However, it is not known how the channel throughput theoretically could change depending on the distance to the transmitter, considering the signal fluctuations. Such a relationship would allow comparing theoretically the calculated throughput data with the experimentally obtained data.

3. SIGNAL POWER LEVEL DEPENDENCE ON THE DISTANCE TO THE TRANSMITTER

As a mobile client moves between Wi-Fi network coverage areas, the association with corresponding wireless AP is established. In Fig. 1, the experimentally observed relationship is shown between the power level *P* of received signal (where *RSS* parameter is used), and the distance to the wireless access point, *r*. The figure shows a mobile client that is moving from AP-1 towards next wireless access point AP-2. P_{d0} is the minimum distance from the client to the AP-1 and P_{TH} is the threshold, at which the mobile client executes a handover procedure to the next AP. It has been observed that as the mobile client moves away from the AP, the power level of the received signal decreases. It has also been observed that the power level of *P* or *RSS* signal not only decreases, but also fluctuates around its average value.

Experimental measurements showed that rapid fluctuations in the *RSS* power levels of the received signal caused irregular (shifted in time) initialization of the handover procedure. It can be executed either too early or with delay, depending on when the P_{TH} or RSS_{TH} value is exceeded. The same applies to the Wi-Fi connection establishment at the initial phase of the measurements. Therefore, when developing handover algorithms, such signal fluctuations must be considered to ensure a correct operation of handover algorithms. Similar experimental observations and related problems have also been described in the study [11].

In this subsection, it is planned to make sure that the experimental observations correspond to the results of theory and other studies [5], [12], [13]. Thus, theoretically the relationship between the changes in the signal power level and the distance to the transmitter will be determined. The data will also be needed in further calculations to determine the maximum theoretical communication channel throughput (capacity).

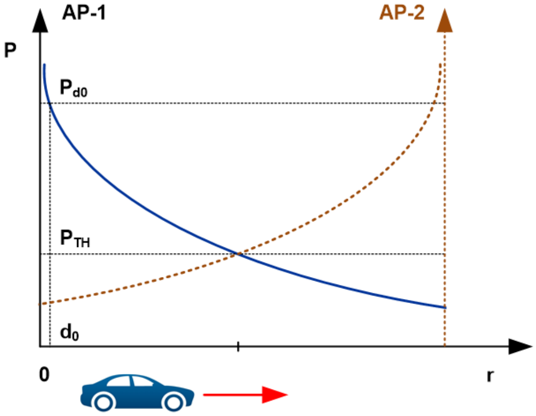

Fig. 1. RSS parameter changes depending on the distance to the transmitter.

The received signal strength describes the received signal power [14].

3.1. Vehicle-to-Infrastructure Communication Channel Model

One of the geometric models of the V2I (Vehicle-to-Infrastructure) communication channel (communication channel between the vehicle and the fixed roadside infrastructure) [15], which takes into account more than one possible signal propagation path, is a two-ray flat-earth model. In this model, the received signal is composed of a directly received signal and a signal reflected from the ground. At short distances, this model gives fast signal fluctuations, because the signal reflected from the ground shifts in and out of phase in relation to the directly received signal. At long distances between the transmitter and the receiver, the direct signal path and ground-reflected signal path become almost the same. According to [15], the boundary between these two areas, d_c is determined by Eq. (1).

$$d_c = \frac{4h_t h_r}{\lambda}, \tag{1}$$

where h_t – height of the transmitting antenna, m (metres); h_r – height of the receiving antenna, m; λ – wavelength, m.

Using Eq. (1) and experimentally obtained data, which are presented in the Table 1, the parameter d_c was calculated, $d_c = 191$ m.

In the two-ray model, random fluctuations are added, the statistics of which depend on the physical scattering of rays in environment, a zero-mean Gaussian distribution is assumed, which gives an acceptable result and is consistent with the results of measurements. This is referred to as a *lognormal* model. The notation of the model in general form is shown in Eq. (2). The model allows determining the power level *P* of the received signal, depending on the distance *r* between the transmitter and the receiver. The present research covers the case where signals propagate over short distances, i.e., if [15], [16].

$$P(r) = P(d_0) - 10u\log_{10}\left(\frac{r}{d_0}\right) + X_\sigma, \tag{2}$$

where *P(r)* – power of the received signal (corresponds to *RSS*) depending on *r*, dBm; d_0 – distance from the wireless access point to the vehicle, m; *r* – distance between a transmitter and a receiver, m; $P(d_0)$ – power of the received signal, when the client is directly opposite of the wireless access point, dBm; *u* – path loss exponent; X_σ – random variables, dB.

Table 1. Experimentally Obtained Data

Parameter	**Value**
h_t	1.85 m
h_r	1.5 m
λ_v	0.058 m
d_0	3.5 m
P(d0)	–49 dBm
r	3.5–100 m
u	1.9
σ	5.9 dB

The values of the parameters *u* and *σ* (where σ – a standard deviation of the random variables X_σ) for the highway case are experimentally obtained in the study [16] and are given in Table 1. In experimental measurements, both the transmitter and receiver used IEEE 802.11ac standard.

3.2. The Power Level of Received Signal without Fluctuations

Using Eq. (2), the values of *P(r)* were calculated without taking X_σ into account. Figure 2 shows the obtained relationship between the power of received signal and the distance from the transmitter to receiver, without signal fluctuations (see a red curve).

3.3. The Power Level of Received Signal with Fluctuations

Due to short distances, which are typical of V2I/V2X (VehicletoEverything) links, a more accurate description of signal fluctuations is given by small-scale fading models, where the fluctuations are caused by constructive and destructive interference between the components of multipath signal propagation. If the in-phase and quadrature components of the signal fluctuate as independent random variables with the Gaussian distribution, the results of *Rayleigh* or *Rician* statistics are provided, depending on whether there is a line of sight. The distribution of the received signal that can be used to model both types of statistics is the Nakagami distribution (3).

$$f(x;\ \alpha,\omega) = \frac{2\alpha^{\alpha}x^{2\alpha-1}}{\omega^{\alpha}\Gamma(\alpha)}e^{\frac{-\alpha x^2}{\omega}}, \tag{3}$$

where *α* is a shape parameter; *ω* is an estimate of average power in the fading envelope; *x* is a general random number that is exposed to the Nakagami distribution.

If *α = 1*, the Nakagami distribution describes a *Rayleigh* distribution, and if *α > 1*, it is the *Rician* distribution. The average value of the fluctuations of the received signal power is calculated as follows:

$$\bar{X}_\sigma = \int_0^\infty x f(x;\ \alpha,\omega)dx = \int_0^\infty x\left(\frac{2\alpha^{\alpha}x^{2\alpha-1}}{\omega^{\alpha}\Gamma(\alpha)}e^{\frac{-\alpha x^2}{\omega}}\right)dx. \tag{4}$$

In the calculations ; thus, Eq. (4) is simplified:

$$\bar{X}_\sigma = \int_0^\infty \frac{2x^2}{\omega} e^{\frac{-x^2}{\omega}} dx. \tag{5}$$

Equation (5) was used to determine the effect of fluctuations of the input signal on *P(r)* (2). In calculations we used *ω* = 1. Initially, the average value of power fluctuations was calculated. Then, random values with Gaussian or Normal distribution were generated, where we used the obtained values and the experimentally obtained standard deviation σ for the random sample variables , which corresponded to the highway scenario (Table 1), [16].

Figure 2 shows the obtained results (see a blue curve).

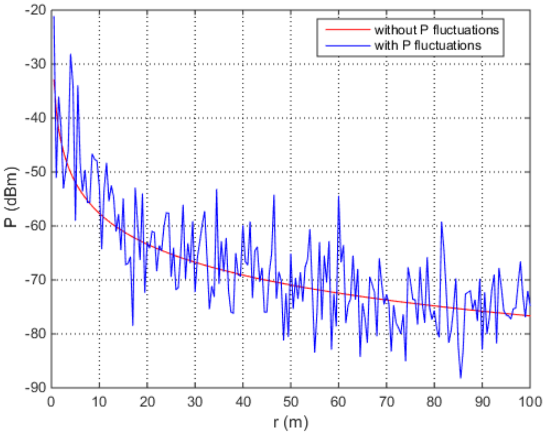

Fig. 2. Theoretically calculated power of the received signal depending on the distance to the transmitter without P fluctuations and with P fluctuations.

4. THROUGHPUT DEPENDENCE ON THE POWER LEVEL OF THE RECEIVED SIGNAL AND THE DISTANCE TO THE TRANSMITTER

The Shannon's frequency channel capacity theorem (Shannon's theorem) is used to calculate the upper limit of data transfer rate of communication channel or the channel capacity *C* (bit/s) (6). It describes the physical layer throughput, which makes it possible to estimate the maximum theoretically obtainable throughput [2], [17]. It represents the ideal system with Gaussian noise [18], [19], where the bit error rate can be reduced to zero by applying appropriate coding schemes, if the user data transfer rate is lower than the channel capacity. However, such codes have not yet been developed, which is one of the reasons why in practice the obtained data transfer rates are several times lower.

$$C = B \log_2\left(1 + \frac{S}{N}\right), \tag{6}$$

where *C* – the capacity of frequency channel, bit/s; *B* – frequency channel bandwidth, Hz; *S* – the average power of the received signal in channel, mW; *N* – the average power of the noise or interference in channel, mW.

By using Eqs. (6) and (2), the theoretical capacity *C* for an ideal communication channel was calculated. In calculations, the parameter values B = 80 MHz and $N = -90$ dBm were used, where the parameter N was converted to mW. The variable S corresponds to $P(r)$ parameter of Eq. (2). The calculated channel capacity C, which changes depending on the received signal power level P, with and without the received signal power level fluctuations, is given in Fig. 3.

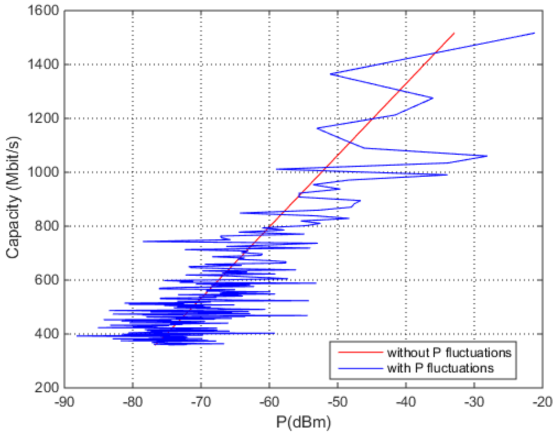

Fig. 3. Theoretically calculated capacity depending on the power P (dBm) of the received signal without and with power fluctuations.

In addition, Fig. 4 shows the theoretically calculated signal power P in mW, depending on the channel capacity C. The parameter P was set in the range of 10^{-9} to 10^{-5} mW, which gives practically achievable results.

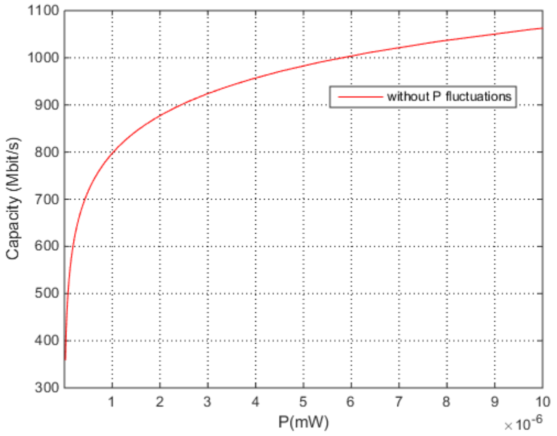

Fig. 4. Theoretically calculated capacity depending on the power P (mW) of the received signal without power fluctuations.

After that theoretical channel capacity C depending on the distance to the transmitter without and with the received signal power level fluctuations was calculated. Theoretically obtained capacity and experimentally obtained goodput results are combined in one graph (see Fig. 5).

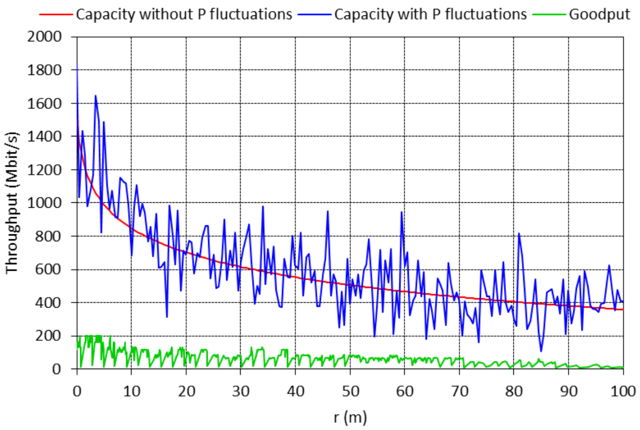

Fig. 5. Theoretically calculated capacity and experimentally obtained goodput depending on the distance to the transmitter.

In Fig. 5, the depicted green curve represents experimentally obtained goodput, where measurement data are taken from Fig. 6 at the velocity of 50 km/h, in the time interval when the mobile client initially is located opposite the AP and then moves away from it by 100 m (in terms of time it corresponds to 7.2 s). The experimental measurements were performed with the standard IEEE 802.11ac client. When the mobile client stays directly opposite AP, the client reaches the maximum goodput, as the client moves away from the AP, the distance *r* increases and the goodput decreases.

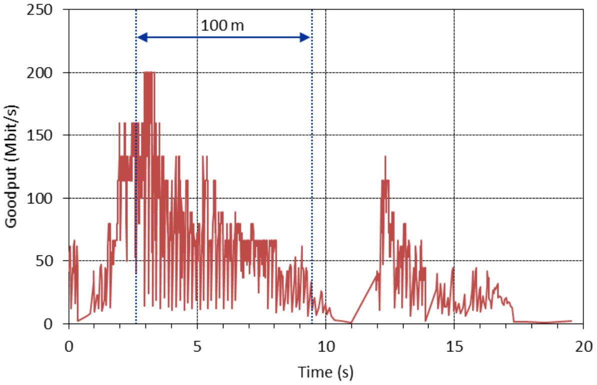

Fig. 6. Experimentally obtained goodput at the velocity of 50 km/h.

5. CONCLUSION

The experimentally obtained results, as well as the theoretically calculated data, show that when a mobile client moves away from the transmitter, the power of the received signal decreases and, as a result, the throughput (capacity and goodput) also decreases. The received signal power is varying and fluctuating in time. The received signal power level fluctuations are caused by constructive and destructive interference between the components of multipath signal propagation. It should be noted that the newly created graphs (Figs. 3–5) are related to idealization, because Shannon's theorem [17], [20] is used in the calculations. The theoretical calculations did not consider the client's speed of movement. The aim of the study has been to make sure whether the experimentally obtained data correspond to the classical conclusions derived from the Shannon's theorem.

Theoretically calculated wireless channel capacity or the maximum possible throughput is several times higher compared to the experimentally obtained goodput (application layer throughput). The trend and nature of curves are similar, but the absolute values are different. Shannon's theorem determines a data transferring rate for an ideal channel at the physical layer. It should be noted that experimental measurements in the case of a stationary wireless network client, where the client's distance to the transmitter would be gradually increased, would give better goodput results compared to a moving client. The WiFi technology used in the study is able to provide experimentally obtained goodput; it can be seen that there is still a large reserve to the theoretical "ceiling". Improving debugging algorithms makes it possible to increase overall network throughput.

Higher layers of the OSI model can recognize data only if they are logically designed. Therefore, e.g., the formation of frames, IP packets and ACK messages are required. If a TCP transport protocol is used, it requires additional tasks for transmitting the data. For instance, during the establishment of a TCP session, a three-way handshake procedure is executed, while in the case of packet loss, data are retransmitted. Each OSI layer (from L7 to L2) generates additional traffic or the overhead, such as information about the used application layer protocol (e.g., FTP), TCP header, IP header, Ethernet header and other communication data that need to be transmitted, and this is not considered in the Shannon's theorem. The performed theoretical calculations justify the experimentally obtained results.

REFERENCES

1. Higginbottom, G.N. (1998). *Performance Evaluation of Communication Networks*. Artech House.
2. Saunders, S.R., & Aragon-Zavala, A. (2007). *Antennas and Propagation for Wireless Communication Systems*. John Wiley & Sons Ltd.
3. Ancans, A., & Petersons, E. (2018). The Relationship between Transport Wireless Network Throughput and Vehicle Speed. *Automatic Control and Computer Sciences (AC&CS), 52* (4), 297–305.
4. Jerjomins, R., Ancans, A., Petersons, E., & Gerina-Ancane, A. (2020). Improving handover mechanism in vehicular WiFi networks. In: *ICTE in Transportation and Logistics 2019*, Lecture Notes in Intelligent Transportation and Infrastructure (ICTE ToL 2019, LNITI), (pp. 243–261). Ginters E., Ruiz Estrada M., Piera Eroles M., eds. Switzerland, Cham: Springer.
5. Sharp, I., & Yu, K. (ed). (2019). *Wireless Positioning: Principles and Practice*. Springer Nature Singapore.
6. Mazuelas, S., ABahillo, A., Lorenzo, R.M., Fernandez, P., Lago, F.A., Garcia, E., … & Abril, E.J. (2009). Robust Indoor Positioning Provided by Real-Time RSSI Values in Unmodified WLAN Networks. *IEEE Journal on Selected Topics in Signal Processing, 3* (5), 821–831.

7. Lim, C.B., Kang, S.H., Cho, H.H., Park, S.W., & Park, J.G. (2010). An Enhanced Indoor Localization Algorithm Based on IEEE 802.11 WLAN Using RSSI and Multiple Parameters. In: *5th International Conference on Systems and Networks Communications* (pp. 238–242), 22 – 27 August 2020, Nice, France.
8. Yamamoto, B., Wong, A., Agcanas, P.J., Jones, K., Gaspar, D., Andrade, R., & Trimble, A.Z. (2019). Received Signal Strength Indication (RSSI) of 2.4 GHz and 5 GHz Wireless Local Area Network Systems Projected over Land and Sea for Near-Shore Maritime Robot Operations. *Journal of Marine Science and Engineering, 7* (9), 290–306.
9. Mouton, M., Castignani, G., Frank, R., & Engel, T. (2015). Enabling Vehicular Mobility in CityWide IEEE 802.11 Networks through Predictive Handovers. *Vehicular Communications, 2* (2), 59–69.
10. Brodsky, M.Z., & Morris, R.T. (2009). In Defense of Wireless Carrier Sense. Conference on Data Communication, *ACM SIGCOMM 2009, 39* (4), 147–158.
11. Hadaller, D., Keshav, S., Brecht, T., & Agarwal, S. (2007). Vehicular opportunistic communication under the microscope. In: *MobiSys '07 Proceedings of the 5th International Conference on Mobile Systems, Applications and Services* (pp. 206–219), 11 – 13 June 2007, San Juan, Puerto Rico.
12. Beard, C., & Stallings, W. (2016). *Wireless Communication Networks and Systems*. Pearson Higher Education, Inc.
13. Svecko, J., Malajner, M., & Gleich, D. (2015). Distance Estimation Using RSSI and Particle Filter. *ISA Transactions, 55*, 275–285.
14. Sauter, M. (2017). *From GSM to LTE – Advanced Pro and 5G. An Introduction to Mobile Networks and Mobile Broadband* (3rd ed.). John Wiley & Sons Ltd.
15. Fei, H. (ed.). (2018). *VehicletoVehicle and VehicletoInfrastructure Communications: A Technical Approach*. CRC Press, Taylor & Francis Group.
16. Emmelmann, M., Bochow, B., & Kellum, C.C. (ed.). (2010). *Vehicular Networking: Automotive Applications and Beyond.* John Wiley & Sons Ltd.
17. Ancans, G., Stafecka, A., Bobrovs, V., Ancans, A., & Caiko, J. (2017). Analysis of Characteristics and Requirements for 5G Mobile Communication Systems. *Latvian Journal of Physics and Technical Sciences, 54* (4), 69–78.
18. Balodis, G. (2011). *Diskrētā signālu apstrāde*. RTU Izdevniecība.
19. Beķeris, E. (2010). *Signālu teorijas pamati*. RTU Izdevniecība.
20. Haykin, S. (2014). *Digital Communication Systems.* John Wiley & Sons, Inc.

sciendo

LATVIAN JOURNAL OF PHYSICS
AND TECHNICAL SCIENCES
2022, N 1

DOI: 10.2478/lpts-2022-0002

SOLAR MICROWAVE EMISSION ASSOCIATED WITH CORONAL MASS EJECTIONS (CME)

J. Kallunki

Aalto University Metsähovi Radio Observatory,
Metsähovintie 114, Kylmälä, 02450, FINLAND
e-mail: juha.kallunki@aalto.fi

The connection between Coronal Mass Ejections (CME) and radio burst has been discovered especially at lower frequencies (< 2 GHz). The aim of the study is to investigate possible connection between CMEs and variability of radio brightenings at 37 GHz (8 mm) within the time frame of four days. The millimetre radio observations have been made on RT-14 radio telescope at Metsähovi Radio Observatory of Aalto University, Finland. In addition, 11.2 GHz (2.7 cm) total solar flux information is included in the analysis. The radio observations were made between March 2011 and September 2017, totally including 24 events. The results demonstrate that in most of the cases the radio brightening intensity achieves its maximum before CME occurs. Time of 11.2 GHz intensity appearance matches with time of CME appearance with difference of two to three hours. However, in most cases a maximum of 11.2 GHz intensity appears before CMEs. The study investigates a possibility of predicting CME appearance based on milli- and centimetre radio observations. The study also proposes a scenario connection between CMEs and solar microwave events.

Keywords: *Coronal Mass Ejection (CME), radio telescope, solar activity, solar radio brightening.*

1. INTRODUCTION

Coronal Mass Ejections (CMEs) are strong eruptive events which are carrying magnetized plasma from the solar atmosphere. CMEs, for instance, are causing geomagnetic storms. Thus, they play a major role in the space weather investigations. They can carry massive kinetic energies, up to 10^{34} erg [1]. The formation of CMEs is not yet comprehensive understood. However, with the current knowledge, they are assumed to be driven by magnetic fields [2]. Also, there have been discussions about the connection between CME and solar flare.

The estimation of CME magnetic fields can be diagnostic based on radio observations [3], [4]. Connection between CMEs and solar radio events has been studied earlier. However, most of the studies have been focusing on lower frequencies (< 2.5 GHz, e.g., [1]–[5]). For instance, connection between solar type II radio burst and CME has been studied in a versatile manner [5].

Type II solar radio bursts are generated by the plasma emission mechanism when electron beams are accelerated ahead of propagating CME [6]. At millimetre wavelength regimes, a comparison to X-ray events has also been investigated [7]. The results show that a gradual thermal component of microwave starts to dominate after the impulsive phase of X-ray flare. CMEs have not been studied at higher radio frequencies. The present article studies the evolution of the radio brightenings at 37 GHz which are associated with CME. The main aim is to find possible connection between CMEs and radio brightenings. For instance, CMEs can be predicted based on radio brightening evolution. The] most common behaviour seems to be that the radio brightening intensity achieves its maximum before the CME occurs. Also, in most cases 11.2 GHz solar radio flux maximum intensity is achieved before CME appears. In Section 2, the used radio instrumentation is shown. Observations are discussed in Section 3 and results – in Section 4. Finally, Section 5 presents conclusions.

2. INSTRUMENTATION

The RT-14 at Metsähovi Radio Observatory (MRO) of Aalto University, Finland (Helsinki region; E 24:23.35, N 60:13.04) is a radome-enclosed Cassegrain-type antenna with a diameter of 13.7 m. The usable wavelength range of the telescope is 13.0 cm–2.0 mm. During solar observations, the antenna is used for solar mapping, partial solar mapping, and tracking of any selected areas on the solar disk. The beam size of the telescope is 2.4 arc min at 37 GHz (8 mm). The receiver is Dicke-type radiometers. For the temperature stabilization, a Peltier element is used. The noise temperature of the 8 mm receiver is approximately 280 K. The temporal resolution during observations is 0.1 s or less. It will take approximately 180 seconds to make one solar radio map.

The observational data are recorded in intensities. Because the measurements are always scaled relative to the quiet Sun level (QSL), the observations are comparable over the years. The brightness temperature of the QSL at 8 mm is 8100 ± **300** K [8].

The full documentation of the RT-14 technical specifications can be found in [9].

The second instrument is a radio telescope with a 1.8 m dish diameter (RT-1.8) dedicated to continuous solar observations. RT-1.8 has measured the total radiation of the Sun since January 2001, at a frequency of 11.2 GHz (2.7 cm). It has been in use for two solar cycles, 23 and 24. The long time series enables solar cyclicity studies. The telescope has a beam size of 81.6 arc min and its system noise temperature, T_{sys}, is 268 K, measured against liquid nitrogen. The radio telescope has no protective radome; therefore, it is vulnerable to prevailing weather conditions. High sampling rate (1 kHz) allows studying fine structure of flares, including short periodic oscillation phenomena. The full documentation of the RT-1.8 technical specifications can be found in [10].

3. OBSERVATION

The radio observations were made between March 2011 and September 2017 and daily maximum brightness temperature value was recorded from daily observed solar raster scan maps. The radio brightenings were associated to NOAA (National Oceanic and Atmospheric Administration) active region, and connection between the active regions and CMEs was found. CME appearance times were collected from HELCATS – The science of tracking solar storms' database (https://www.helcats-fp7.eu). The CME appearance time is defined so when CME is first time observed in HI1 camera (wide-field white-light camera). The maximum radio brightening temperature values were taken during the period of four days, starting two days before CME occurred and stopping one day after CME occurred. Figure 1 presents the evolution of radio brightening between 4 September 2017 and 7 September 2017.

In the third plot (in lower left panel, radio map from 6 September 2017), we can notice that a radio brightening area is expanding compared to other days. In addition, the intensity is stronger. CME appeared on 6 September 2017.

Number of daily solar radio maps varied widely. On certain days, we only had one to three radio maps, but on some days we had more than two hundred radio maps. On the days with a dense sampling, we recorded the radio brightening intensity simultaneously when CME appeared. However, on days with a sparse sampling, we had rough estimate on its intensity. Thus, we probably missed the radio brightening intensity when CME appeared.

Totally, we found 24 events (Table 1), where we had both radio brightening and CME observations. In some cases, there were several CMEs during this period of four days. CMEs under investigation were chosen that the CME observation was classified into class "good". It means that eruption is defined with a good confidence as CME. The selection of the events was made based on radio brightenings. Even though there were more CME events in the period under review, we were missing the radio data on those events. Ground-based radio data are also certainly available only from the sunrise to the sunset. MRO-14 radio telescope is also used for other purposes than solar observations. Thus, we have only one solar radio map for each day.

Table 1. CMEs and Radio Brightness Maxima (11 and 37 GHz) Occurrence Time
(including radio brightness maximum intensities relative to the QSL)

CME occurrence time	37 GHz max. intensity occurrence time	37 GHz max. intensity (rel. to QSL)	11 GHz max. intensity occurrence time	11 GHz max. intensity (rel. to QSL)
2011-03-07-14:48	2011-03-07 10:19	105.1	2011-03-07 09:20	149.1
2011-03-14 16:09	2011-03-14 09:44	104.4	No detection	No detection
2011-04-17 14:09	2011-04-17 12:16	111.1	No detection	No detection
2011-06-02 10:49	2011-06-02 14:11	106.9	No detection	No detection
2011-06-07 06:49	2011-06-07 04:19	105.6	2011-06-07 06:25	181.8
2011-06-23 19:29	2011-06-23 03:57	105.4	No detection	No detection
2011-07-09 04:09	2011-07-09 10:34	104.3	No detection	No detection
2011-08-02 10:49	2011-08-02 03:52	112.3	2011-08-02 06:10	121.8
2011-08-30 15:29	2011-08-03 04:00	137.9	2011-08-03 13:30	129.1
2011-08-04 05:29	2011-08-04 03:42	124.2	2011-08-04 03:55	192.3
2011-08-09 09:29	2011-08-09 10:52	105.2	2011-08-09 08:05	192.3
2012-05-16 10:09	2012-05-16 04:07	105.1	No detection	No detection
2012-05-17 06:09	2012-05-17 04:00	106.5	No detection	No detection
2012-06-13 15:29	2012-06-13 04:08	109.8	2012-06-13 13:35	110.9
2013-04-11 09:29	2013-04-11 11:05	111.9	2013-04-11 07:10	129.6
2013-05-01 06:09	2013-05-01 04:36	110.4	2013-05-01 14:10	103.7
2013-05-17 10:49	2013-05-17 09:32	140.2	2013-05-17 08:55	181.8
2013-06-05 05:29	2013-06-05 05:01	103.8	2013-06-05 08:35	124.5
2013-08-06 07:29	2013-08-06 04:11	105.0	No detection	No detection
2013-08-17 12:09	2013-08-17 06:11	105.5	No detection	No detection
2014-09-03 06:09	2014-09-03 04:33	106.7	2014-09-03 13:35	131.9
2016-07-17 14:49	2016-07-17 08:21	114.6	No detection	No detection
2017-05-06 08:49	2017-05-06 09:37	102.7	No detection	No detection
2017-09-06 14:09	2017-09-06 09:38	198.4	2017-09-06 12:00	222.2

In addition, 11.2 GHz solar intensity was considered. CME occurrence time and 11.2 GHz solar intensity maximum occurrence time had not longer than three hours of cadence. Figure 2 presents 11.2 GHz solar total flux on 6 September 2017. There were three radio bursts before CME appeared. CME appeared on a gradual state of the third burst. Figures 3 and 4 show other examples. These observations were made between 31 July and 3 August 2011. During this period, several CMEs appeared.

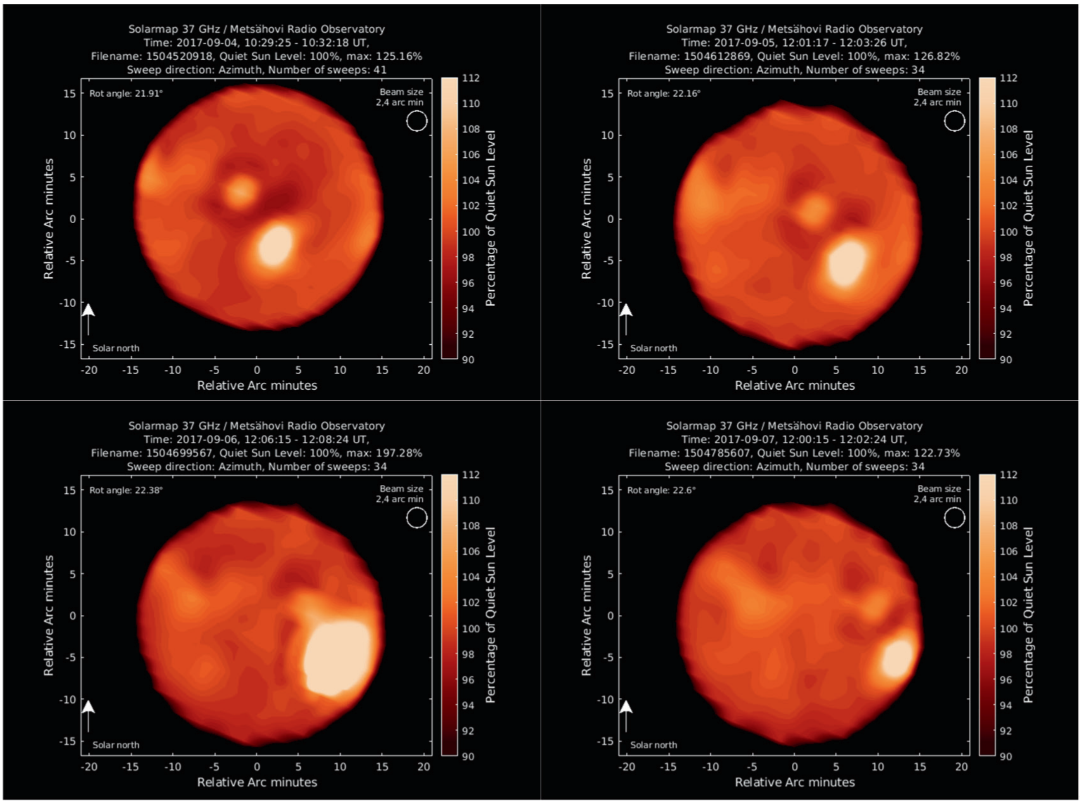

Fig. 1. Evolution of radio brightening between 4 September 2017 (upper left panel) and 7 September 2017 (lower right panel). Radio brightening size and intensity are on top on 6 September 2017 (lower left panel).

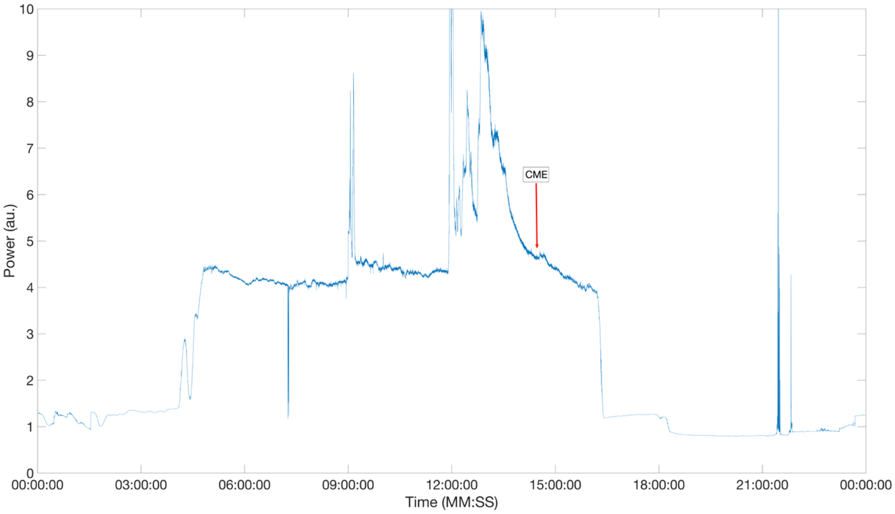

Fig. 2. The solar total intensity at 11.2 GHz on 6 September 2017. CME appearrence time is indicated with an arrow.

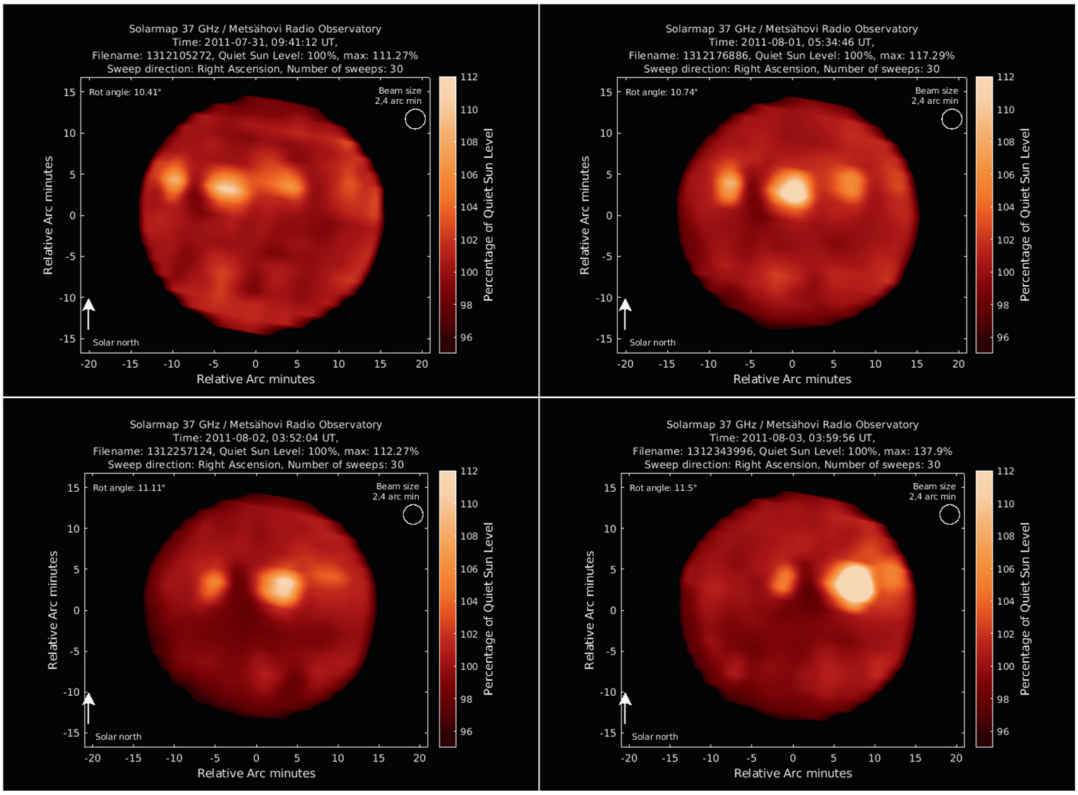

Fig. 3. Evolution of radio brightening between 31 July 2011 (upper left panel) and 3 August 2011 (lower right panel). Radio brightening size and intensity are on top on 3 August 2011 (lower right panel), one day after the CME appeared. This is explained by the fact that there was another CME on 3 August 2011. A weak solar burst appeared after CME.

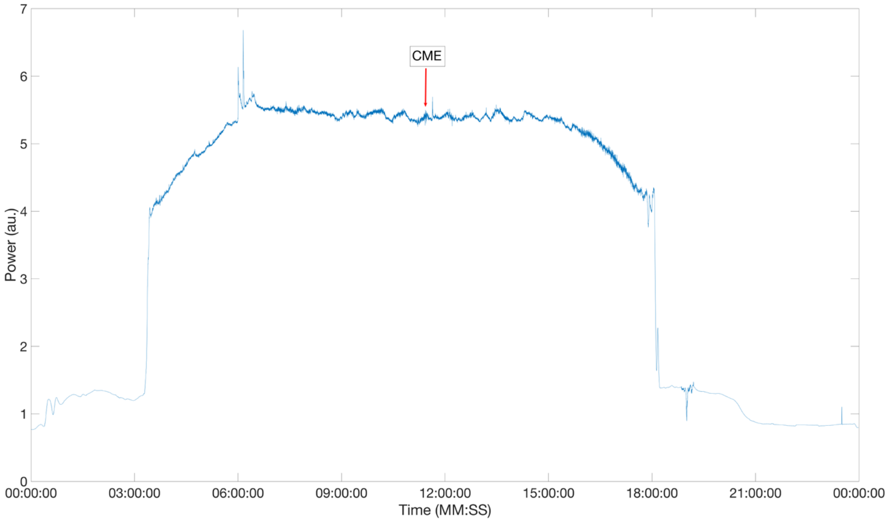

Fig. 4. The solar total intensity at 11.2 GHz on 2 August 2011. CME appearance time is indicated with an arrow.

4. RESULTS

Based on high radio frequency (37 GHz) observations, the obtained results can be divided into four different categories:

- Category 1 – The maximum radio intensity is achieved after the CME occurs. Totally 8 cases.
- Category 2 – The maximum radio intensity is achieved before the CME occurs. Totally 14 cases.
- Category 3 – The maximum radio intensity is achieved simultaneously when the CME occurs. One case.
- Category 4 – No clear pattern/or not enough observations. One case.

The high frequency (37 GHz) radio brightenings of Category 2 (average 122 % to QSL) were stronger than those of Category 1 (average 114 % to QSL).

In addition, we noticed that CME and 11.2 GHz radio burst intensity maximum appeared within two to three hours. We could not detect 11.2 GHz burst in every 24 cases. In nine cases of thirteen, 11.2 GHz solar radio burst maximum intensity was detected before CME appeared. It has been reported [11] that CMEs appear between 15 and 30 minutes after flares appear. Most probably 11.2 GHz burst was detected in Category 1 (5/8) than in Category 2 (7/14). The radio intensity at 11.2 GHz was stronger in Category 2 (> 165 % to QSL) than in Category 1 (120 % to QSL). Some events belonging to Category 2 were so strong that even the receiver signal chain saturated. Therefore, more precise intensity average value cannot be defined.

The intensity of 11.2 GHz bursts was weaker in those events, which appeared after CME (120 % to QSL). The average intensity of those events, which were observed before CME, was > 145 % to QSL. Finally, when we compared millimetre and centimetre wavelength observations to each other, we noticed that centimetre range (2.7 cm) radio burst was detected more probably when radio brightening intensity (at 37 GHz) was strong.

5. CONCLUSIONS

It has been proposed that CME energies correlate with solar flare appearance. In practice, more intense and energetic CMEs produce solar flares. This scenario also holds for solar radio bursts. Lower frequency (11.2 GHz) radio observations give a reason to speculate that radio burst is a triggering for CME. If a strong radio burst is detected, it is highly possible that CME is following it. Below, a simplified scenario is presented based on our observations.

We will need more observations to confirm our interpretation, especially at lower frequencies. We could utilise, for instance, LOFAR (Low-Frequency Array) observations for this purpose. In addition, more densely sampled intensity profile of radio brightening could give additional information to our scenario. During the next solar cycle, cycle 25, we will try to observe more these events with a more densely sampled interval.

ACKNOWLEDGEMENTS

This publication makes use of data obtained at Metsähovi Radio Observatory of Aalto University. We acknowledge support from the European Union FP7-SPACE-2013-1 programme for the HELCATS project (#606692).

REFERENCES

1. Cecatto, J. R. (2009). Observations of Radio Spectra at 1–2.5 Ghz Associated with CME Start Time. *Universal Heliophysical Processes, 257,* 317–321. doi:10.1017/S1743921309029482.
2. Aschwanden, M. J. (2004). *Physics of the Solar Corona. An Introduction*. Berlin: Springer.
3. Isaeva, E. A., & Tsap, Y. T. (2017). Microwave Emission of Solar Flares: Coronal Mass Ejections and Shock Waves. *Odessa Astronomical Publications, 30*, 222. doi:10.18524/1810-4215.2017.30.114670.
4. Mondal, S., Oberoi, D., & Vourlidas, A. (2020). Estimation of the Physical Parameters of a CME at High Coronal Heights Using Low-frequency Radio Observations. *The Astrophysical Journal, 893* (1). doi:10.3847/1538-4357/ab7fab.
5. Dididze, G. (2019). Comparative Analysis of Solar Radio Bursts before and during CME Propagation. *Astronomy and Astrophysics, 625*. doi:10.1051/0004-6361/201629489.
6. Krupar, V. (2019). Statistical Survey of Coronal Mass Ejections and Interplanetary Type II Bursts. *The Astrophysical Journal, 882* (2). doi:10.3847/1538-4357/ab3345.
7. Pohjolainen, S., Hildebrandt, J., Karlický, M., Magun, A., & Chertok, I. M. (2002). Prolonged Millimeter-Wave Radio Emission from a Solar Flare Near the Limb. *Astronomy and Astrophysics, 396*, 683–692. doi:10.1051/0004-6361:20021431.
8. Kallunki, J., & Tornikoski, M. (2018). Measurements of the Quiet-Sun Level Brightness Temperature at 8 mm. *Solar Physics, 293* (11), article id. 156.
9. Kallunki, J., Tornikoski, M., Tammi, J., Kinnunen, E., Korhonen, K., Kesäläinen, S., & Arkko, O. (2018). Forty Years of Solar Radio Observations at Metsähovi Radio Observatory. *Astronomische Nachrichten, 339* (204), 204–211.
10. Uunila, M., & Kallunki, J. (2015). Reliability of 1.8-Meter Solar Radio Telescope at Metsähovi Radio Observatory for Long-term Solar Monitoring. *Astrophysics and Space Science, 359*, article id. 33.
11. Youssef, M. (2013). Statistical Study of the CME-Solar Flares Associated Events. *Earth Moon and Planets, 110* (3–4), 185–195. doi:10.1007/s11038-013-9419-1.

LATVIAN JOURNAL OF PHYSICS
AND TECHNICAL SCIENCES
2022, N 1

DOI: 10.2478/lpts-2022-0003

THE RELATION BETWEEN PHOTOCONDUCTIVITY THRESHOLD AND OPEN-CIRCUIT VOLTAGE IN ORGANIC SOLAR CELLS

R. Grzibovskis[1*], A. Ruduss[2], A. Polaks[1]

[1] Institute of Solid State Physics, University of Latvia,
8 Kengaraga Str., Riga, LV-1063, LATVIA
[2] Faculty of Materials Science and Applied Chemistry,
Riga Technical University,
3/7 P. Valdena Str., Riga, LV-1048, LATVIA
*E-mail: raitis.g@cfi.lu.lv

Most of the solar cell parameters (short-circuit current, fill factor, power conversion efficiency) can only be determined by creating and measuring the solar cell. However, there is an empirical relation that links energy level values of the materials in the active layer to an open-circuit voltage (U_{oc}) of the solar cell. Due to a variety of possible methods used to determine energy level values and the dispersion of obtained results, this estimate is not always correct. Even if correct energy level values are obtained for separate materials, energy level shift takes place at the interfaces when two materials are mixed. That is why a simple and reliable experimental method for U_{oc} estimation is required. Usually, photoconductivity is used to obtain the energy gap between molecule ionization energy and electron affinity of a single material. When two materials are mixed, direct charge transfer from donor to acceptor molecule can be observed. The threshold energy (E_{CT}) shows the real difference between donor molecule ionization energy and acceptor molecule electron affinity. This difference should correspond to the U_{oc}. The present study makes the comparison between the open-circuit voltage estimated from material energy level values, the obtained E_{CT} values for various donor:acceptor systems, and the real U_{oc} obtained from solar cell measurements. Strong correlation between E_{CT} and U_{oc} is obtained and the photoconductivity measurements can be used in the estimation of U_{oc}.

Keywords: *Energy levels, direct charge transfer, open-circuit voltage, organic materials, organic solar cells, photoconductivity.*

1. INTRODUCTION

Environmental concerns compel many nations to develop technologies that allow collecting renewable energy and decreasing the use of fossil fuels. Solar cells allow directly turning the sunlight into electricity. The wide variety of organic materials combined with the possibility to vary their molecule structure makes them an attractive field of research. The efficiency of organic solar cells is steadily increasing and nowadays reaches 18 % [1]. Solar cells are characterised by several parameters, such as short-circuit current (I_{sc}), open-circuit voltage (U_{oc}), fill factor (FF), and power conversion efficiency (PCE) [2], [3]. All previously mentioned parameters are affected not only by the properties of each separate material but also by material compatibility. I_{sc} depends on two factors: the efficiency of charge carrier generation in the active layer, and the efficiency of charge carrier extraction from the solar cell. U_{oc} is mainly defined by the energy levels of the materials used in the active layer. The prediction of open-circuit voltage is based on the empirical relation that consists of donor and acceptor molecule energy levels:

$$U_{oc} = {}^{1}\!/_{e}\left(I_d - E_{a,a}\right) - 0.3V, \quad (1)$$

where e is the elementary charge, I_d is the molecule ionization energy of the electron donor material, and $E_{a,a}$ is the electron affinity of the electron acceptor material [4]. Equation (1) is simple and would potentially allow us to estimate the most promising donor:acceptor combination without the need of time- and resource-consuming solar cell manufacturing. That is why the correct determination of energy level values is crucial. The most common method for molecule ionization energy determination is ultraviolet photoelectron spectroscopy (UPS) [5], [6]. Photoelectron yield spectroscopy (PYS) is used as an alternative method [7]–[10] as it is simple and does not require an ultrahigh vacuum. Although the principle of these methods is similar, reported results can differ from author to author. For example, ionization energy values for popular electron donor polymer poly(3-hexylthiophene-2,5-diyl) (P3HT) in various scientific papers ranges from 4.7 to 5.3 eV [11]–[15]. In our previous studies, we obtained the value of 4.54 ± 0.03 eV [9], [10]. Correct estimation of electron affinity is even more complicated. Although it can be directly determined using inverse photoemission spectroscopy (IPES) [16], [17], due to the poor energy resolution and complexity of the method, IPES is rarely used. Usually, the electron affinity value is obtained indirectly from molecule ionization energy and energy gap measurements. The energy gap between molecule ionization energy and electron affinity can be estimated either from absorption edge or from photoconductivity measurements [18]. A relatively popular method for the energy level estimation of organic semiconductors in solution is cyclic voltammetry. Yet there is still debate about the validity and precision of this method [19], [20].

Additionally, it has been shown that the energy level shift takes place at the organic material interface [10], [21], [22]. It means that even if the correct energy level values for each separate material are obtained, the real gap between donor molecule ionization energy and acceptor material electron affinity can differ from the estimated value when materials are mixed. In that case, the predicted U_{oc} value may differ from the real value. That is why a simple, reliable, and direct method is needed for the correct prediction of U_{oc}.

In the photogeneration process, the donor molecule is excited by the absorption of a photon. In the next step, the electron is transferred to the acceptor molecule [3]. It is also possible to transfer electron directly from the donor molecule to the acceptor molecule without the excitation of the donor molecule. This process is called direct charge transfer (CT). The energy of this transition shows the real energy gap between the ionization energy of donor material and the electron affinity of acceptor material at the interface. While this energy could be determined optically by measuring the absorption or luminescence spectra [23], [24], it is a complicated task due to the low probability of CT transition. In these measurements, the signal is small and is close to the sensitivity threshold of the equipment. Alternatively, CT transition can be observed in photoconductivity measurements [25]. Usually, photoconductivity measurements are used to obtain the energy gap between the ionization energy and electron affinity of a single material. When two materials are mixed creating bulk heterojunction, the photoconductivity threshold shows the lowest energy required to transfer an electron from the donor molecule to the acceptor molecule. This could allow us to evaluate the real gap between energy levels in the system and to predict the maximum obtainable voltage of solar cells more precisely. This study aims to show the relation between CT energy obtained from photoconductivity measurements, prediction of U_{oc} based on the measured energy levels of studied materials, and the real open-circuit voltage of created solar cells. Photoconductivity measurements are done for various donor:acceptor mixtures. The obtained threshold values are compared to the U_{oc} obtained from solar cells using the same donor:acceptor combinations.

2. EXPERIMENTAL

2.1. Studied Materials

In this study, commercially available organic materials, as well as original materials synthesized at Riga Technical University are studied. The chosen materials are either well-known compounds used in the efficient solar cells (P3HT, PCBM, PBDB-T, Y5, PCDTBT, PCPDTBT) or promising original compounds created in previous studies (DC-1, DC-2, DZC-3). Molecule structures are shown in Fig. 1. Commercially available materials are obtained from Sigma-Aldrich. The synthesis of DC-1 and DC-2 has previously been described in [26], while the synthesis of DZC-3 has been described in [27].

Sample Preparation

Three series of samples were made:

1. samples for energy level determination;
2. samples for CT measurements;
3. photovoltaic cells for U_{oc} determination.

Samples for energy determination were made on etched ITO covered glass (Präzisions Glas and Optik GmbH). Solutions in chloroform with the concentration of 15–20 mg/ml were prepared and spin-coated at the speed of 600 rpm, acceleration of 600 rpm/s, and spinning time of 40 s. Afterward, the samples were dried on a hotplate for 15 min at 70 °C. The thickness of samples was between 500 and 700 nm. These samples were used in PYS measurements to obtain the ionization energy of the studied materials. After the ionization energy measurements, 30 nm thick semitransparent aluminum (Al) electrodes were deposited on top of the organic layer by thermal evaporation in a vacuum (~$1\cdot10^{-5}$ mbar) using Edwards Auto 306 thermal evaporator. The obtained "sandwich" type samples (ITO/studied material/ Al) were used for photoconductivity measurements.

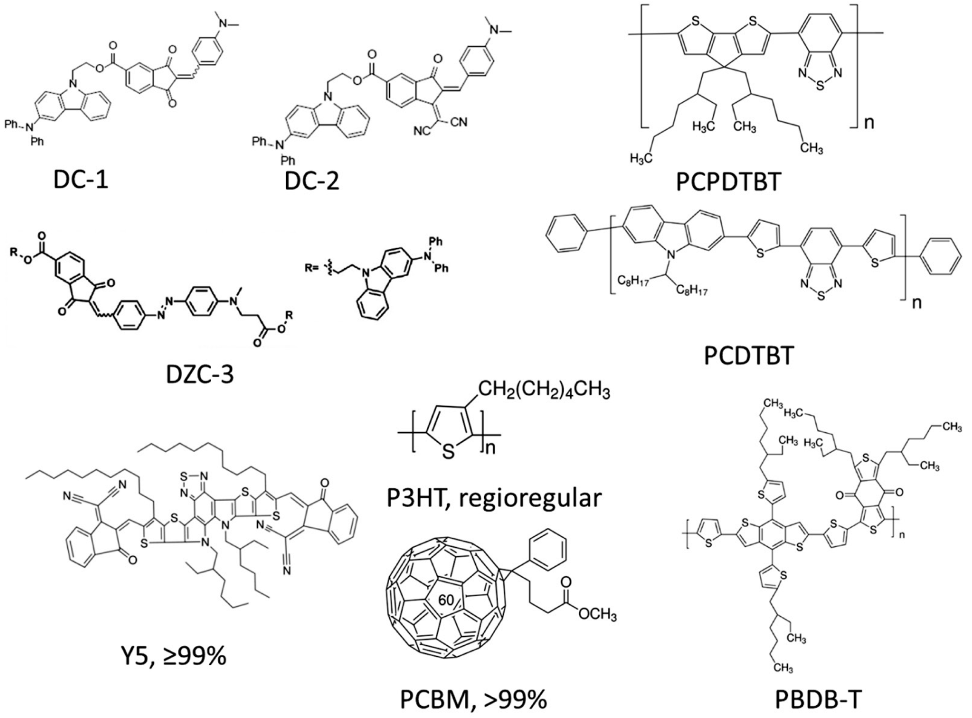

Fig. 1. Molecule structures of studied materials.

Samples for CT measurements were from solutions where the studied materials were dissolved in chloroform with a concentration of around 15 mg/ml. Then two solutions were mixed with the mass ratio of 1:1. The obtained mixtures were spin-coated at the speed of 600 rpm, acceleration of 600 rpm/s, and spinning time of 40 s, obtaining bulk heterojunction thin films. Afterward, the samples were dried on a hotplate for 15 min at 70 °C. 30 nm Al electrodes were deposited on top of the film by thermal evaporation in vacuum using Edwards Auto 306 thermal evaporator. The structure of samples was ITO/ donor:acceptor/ Al.

Solar cells with the structure of ITO/ PEDOT:PSS/ donor:acceptor/ LiF/ Al were made. The layers were deposited on etched indium tin oxide (ITO) glass (Präzisions Glas and Optik GmbH). At first, PEDOT:PSS (Al4083) was spin-coated at the speed of 2000 rpm, acceleration of 2000 rpm/s, and spinning time of 60 s. Afterward, the samples were dried on a hotplate for 15 min at 120 °C. Solutions in chloroform with the concentration of 6 mg/ml of the studied materials were used. Various donor:acceptor combinations were prepared by mixing two solutions with the mass ratio of 1:1. The obtained mixtures were spin-coated in a glovebox in an argon atmosphere. Spin-coating parameters were the following: rotation speed of 1000 rpm, acceleration of 1000 rpm/s, and spinning time of 40 s. The samples were dried on a hotplate for 15 min at 70 °C. 1 nm LiF and 100 nm Al were deposited using Moorfield Nanotechnology MiniLab LT090A-MX thermal evaporator in Jacomex glovebox. Al deposition rate was 0.3 nm/s.

2.2. Measurements

Photoelectron emission measurements were done in a vacuum (~$2\cdot10^{-5}$ mbar) using a self-built measurement system. ENERGETIQ Laser-Driven Light Source (LDLS EQ-99) was used as a light source. Spectral Products DK240 1/4m monochromator was used to control the energy of photons reaching the sample. The spectral range of these measurements was between 4.0 and 6.8 eV with a step of 0.05 eV. Cylindrical lens before the quartz window of the vacuum chamber ensured irradiation area of 5x 10 mm of the sample area. A copper electrode located 2 cm away from the sample was used to collect the emitted electrons. Keithley 617 electrometer was used as a voltage source as well as the equipment for electric current measurements. A voltage of 50 V was applied between electrode and sample to improve the obtained electrical signal. Detailed experimental procedure and data processing has been previously described in [9].

The setup for photoconductivity measurements was similar to that used in photoelectron emission experiments. Here, a short focal length spherical lens was used to focus the light on around 1x 1 mm surface area. Thin films were irradiated through the deposited semitransparent Al electrode and the electrical current between Al and ITO electrodes was measured. In the case of pure materials where photoconductivity was used to determine the energy gap between their molecule ionization energy and electron affinity, the spectral range depended on their absorption spectrum. In the case of mixed samples for CT measurements, the chosen region was wider starting in the infrared part of the spectrum at 2100nm (0.59 eV photon energy). The generated current was measured with Keithley 617 electrometer. Photocurrent spectral dependence was measured with a step of 5 nm. Data processing was done according to [18]. From photoconductivity measurements, the gap (E_{gap}) between ionization energy and electron affinity (E_a) was obtained for each of the studied materials. Knowing the ionization energy and the gap energy, electron affinity was calculated as follows:

$$E_a = I - E_{gap}. \tag{2}$$

Photovoltaic effect measurements were done using Keithley 6517B electrometer. A solar simulator ScienceTech SS150 with a light intensity of 100 mW/cm^2 and a standard AM 1.5 filter was used as a light source. Current–voltage characteristics were measured with a step of 0.02 V. Point in current–voltage characteristics where the electrical current value is closest to 0 A is considered U_{oc}.

3. RESULTS AND DISCUSSION

Although the energy level values for commercial compounds were available in the literature, the ionization energy and electron affinity were measured for all the studied materials. It was done to ensure that all the values were obtained using the same method in the same conditions. The values summarised in Table 1 were used to estimate the $U_{oc,est}$ value for various donor:acceptor material combinations according to Eq. (1).

Table 1. Studied Materials and Their Energy Level Values

Material	**I, eV ±0.03 eV**	**E_a,eV ±0.05 eV**
P3HT	4.54	2.79
PCBM	6.08	3.63
PBDB-T	4.87	3.15
Y5	5.55	3.87
PCDTBT	5.10	3.40
PCPDTBT	4.90	3.60
DC-1	5.16	3.36
DC-2	5.15	3.48
DZC-3	5.13	3.41

For separate materials, the photoconductivity threshold defines the gap between molecule ionization energy and electron affinity. It means that by increasing the photon energy near the gap energy, the measured photocurrent rapidly increases even by several orders of magnitude. Below the E_{gap} there is usually no photoconductivity or small signal generated by the impurities in the film. As an example, P3HT and DZC-3 photoconductivity spectral dependence is shown in Fig. 2a. Although the E_{gap} for both of these materials is similar (1.75 for P3HT and 1.72 for DZC-3), it can be seen that there is a small photocurrent till around 1.4 eV for P3HT, while no photoconductivity could be observed below 1.6 eV for DZC-3.

When mixed, a photoconductivity signal can be observed in the infrared spectral region starting from 0.80 eV (see Fig. 2a). Here, the photon energy is too low to directly excite any of the studied materials and we observe direct charge transfer from P3HT to DZC-3. The probability of direct CT is low and the obtained signal near the threshold energy is almost 4 orders of magnitude lower than the signal of classical photoconductivity. Similar photoconductivity spectral dependence can be observed for other electron donor and acceptor combinations (see Fig. 2b). In all cases, the observed photoconductivity threshold energy for mixtures is lower than the threshold energy for separate materials.

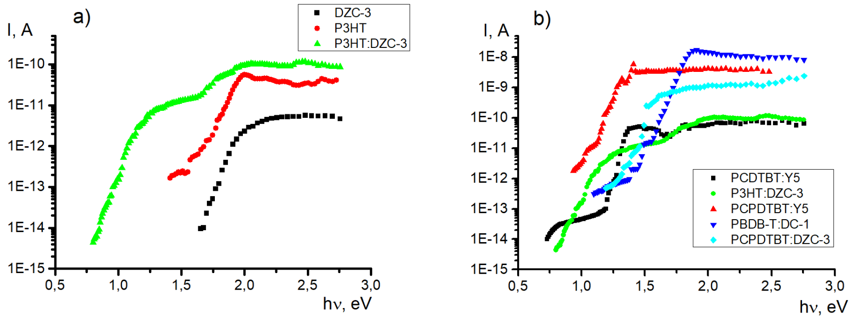

Fig. 2. Photocurrent spectral dependence for
a) DZC-3, P3HT, and P3HT:DZC-3 sample; b) various donor:acceptor mixtures.

The estimated $U_{oc,est}$ values, and CT threshold values (E_{CT}) for various donor:acceptor combinations were compared to the real U_{oc} values obtained from photovoltaic effect measurements of created solar cells. The error for $U_{oc,est}$ is ±0.08 V due to the errors of energy level value determination, the error of U_{oc} is ±0.02 V as a measurement step, and the error of E_{CT} is ±0.03 eV. As can be seen in Fig. 3, the correlation between estimated and real open circuit voltage values is moderate. The trend is generally the same – the higher the estimated $U_{oc,est}$, the higher the real value. Nevertheless, the data are scattered and in several cases, there is an immense overestimation. Linear approximation of $U_{oc,est}$ gives a correlation coefficient of r=0.61, which is considered a moderate correlation.

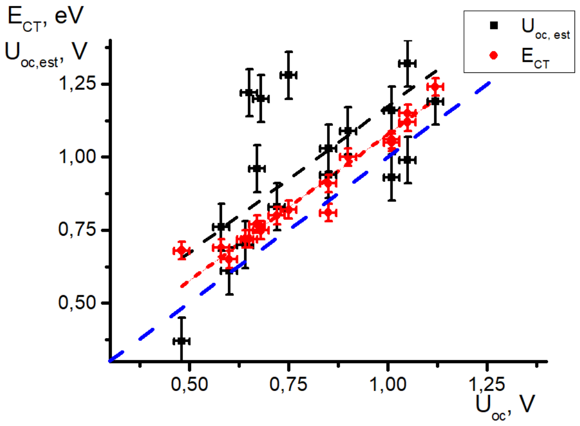

Fig. 3. The E_{CT} and $U_{oc,est}$ comparison to U_{oc}. Black dashed line is a linear approximation of $U_{oc,est}$ values; red dashed line is a linear approximation of E_{CT} values; the blue dashed line shows a perfect fit.

The photoconductivity threshold values are less scattered and are closer to the U_{oc} values. Linear approximation of the results gives a relation between E_{CT} and U_{oc}:

$$U_{oc} = E_{CT} - 0.08\ V. \quad (3)$$

The slight overestimation of E_{CT}, especially towards the lower U_{oc} values, could be related to the sensitivity of the measurements. The signal-to-noise ratio and thus the precision of the measurements could be improved by a light source with higher intensity in the infrared region of the spectrum. Also, the quality of the samples can greatly influence the stability and sensitivity of the measurements. The correlation coefficient, in this case, is r=0.96 which shows a very strong correlation between photoconductivity threshold energy and U_{oc} values.

4. CONCLUSIONS

We have shown that the estimation of open-circuit voltage should not be based only on energy level values obtained from bulky films of pure materials. Using relatively simple photoconductivity measurements, we were able to get direct CT threshold energy which corresponded to the real energy gap between molecule ionization energy of electron donor and electron affinity of electron acceptor material. Although this threshold value slightly overestimates the real U_{oc} value, the deviations are smaller compared to the $U_{oc,est}$ obtained from energy level values.

ACKNOWLEDGEMENTS

Financial support provided by Scientific Research Project for Students and Young Researchers No. SJZ/2020/08 implemented at the Institute of Solid State Physics, University of Latvia is greatly acknowledged. Institute of Solid State Physics, University of Latvia as the Centre of Excellence has received funding from the European Union's Horizon 2020 Framework Programme H2020-WIDESPREAD-01-2016-2017-TeamingPhase2 under grant agreement No. 739508, project CAMART².

REFERENCES

1. Liu, Q., Jiang, Y., Jin, K., Qin, J., Xu, J., Li, W. … & Ding, L. (2020). 18% Efficiency Organic Solar Cells. *Sci. Bull., 65*, 272–275. doi:10.1016/j.scib.2020.01.001.
2. Qi, B., & Wang, J. (2013). Fill Factor in Organic Solar Cells. *Phys. Chem. Chem. Phys., 15*, 8972–8982. doi:10.1039/c3cp51383a.
3. Deibel, C., & Dyakonov, V. (2010). Polymer-Fullerene Bulk Heterojunction Solar Cells. *Reports Prog. Phys., 73*. doi:10.1088/0034-4885/73/9/096401.
4. Scharber, M.C., Mühlbacher, D., Koppe, M., Denk, P., Waldauf, C., Heeger, A.J., & Brabec, C.J. (2006). Design Rules for Donors in Bulk-Heterojunction solar Cells - Towards 10 % Energy-Conversion Efficiency. *Adv. Mater., 18*, 789–794. doi:10.1002/adma.200501717.
5. Chandekar, A., & Whitten, J.E. (2005). Ultraviolet Photoemission and Electron Loss Spectroscopy of Oligothiophene Films. *Synth. Met., 150,* 259–264. doi:10.1016/j.synthmet.2005.02.013.
6. Casu, M.B., Imperia, P., Schrader, S., & Falk, B. (2001). Ultraviolet Photoelectron Spectroscopy of Thin Films of New Materials for Multilayer Organic Light Emitting Diodes. *Surf. Sci., 482–485,* 1205–1209. doi:10.1016/S0039-6028(01)00733-6.
7. Honda, M., Kanai, K., Komatsu, K., Ouchi, Y., Ishii, H., & Seki, K. (2007). Atmospheric Effect of Air, N2, O2, and Water Vapor on the Ionization Energy of Titanyl Phthalocyanine Thin Film Studied by Photoemission Yield Spectroscopy. *J. Appl. Phys., 102*. doi:10.1063/1.2809360.
8. Monjushiro, H., Watanabe, I., & Yokoyama, Y. (1991). Ultraviolet Photoelectron Yield Spectra of Thin Gold Films Measured in Air. *Anal. Sci., 7,* 543–547. doi:10.2116/analsci.7.543.
9. Grzibovskis, R., & Vembris, A. (2016). Study of the P3HT/PCBM Interface Using Photoemission Yield Spectroscopy. *Org. Photonics, 7*, 98950Q. doi:10.1117/12.2227823.
10. Grzibovskis, R., & Vembris, A. (2018). Energy Level Determination in Bulk Heterojunction Systems Using Photoemission Yield Spectroscopy: Case of P3HT:PCBM. *J. Mater. Sci., 53*, 7506–7515. doi:10.1007/s10853-018-2050-9.
11. Wang, Y., Chen, J., Do Kim, H., Wang, B., Iriguchi, R., & Ohkita, H. (2018). Ternary Blend Solar Cells Based on a Conjugated Polymer with Diketopyrrolopyrrole and Carbazole Units. *Front. Energy Res., 6*, 1–9. doi:10.3389/fenrg.2018.00113.

12. Hou, J., & Guo, X. (2013). Active Layer Materials for Organic Solar Cells. *Green Energy Technol., 128*, 17–42. doi:10.1007/978-1-4471-4823-4_2.
13. Li, J., Liang, Z., Peng, Y., Lv, J., Ma, X., Wang, Y., … & Xia, Y. (2018). 36% Enhanced Efficiency of Ternary Organic Solar Cells By Doping a NT-Based Polymer as an Electron-Cascade Donor. *Polymers (Basel), 10*. doi:10.3390/polym10070703.
14. Wu, J., Yue, G., Xiao, Y., Lin, J., Huang, M., Lan, Z., … & Sato, T. (2013). An Ultraviolet Responsive Hybrid Solar Cell Based on Titania/Poly(3- Hexylthiophene). *Sci. Rep., 3*. doi:10.1038/srep01283.
15. Safriani, L., Risdiana, R., Fitrilawati, F., Manawan, M., Bahtiar, A., Aprilia, A., … & Watanabe, I. (2018). Charge Carrier Transport in Blend of P3HT and ZnO Nanoparticles at Low Temperature Studied by μsR. *J. Phys. Conf. Ser., 1080*, 0–5. doi:10.1088/1742-6596/1080/1/012011.
16. Hill, I.G., Kahn, A., Soos, Z.G., & Pascal, R.A. (2000). Charge-Separation Energy in Films of π -Conjugated Organic Molecules. *Chem. Phys. Lett., 327*, 181–188. doi:10.1016/S0009-2614(00)00882-4.
17. Fahlman, A., Hamrin, K., Hedman, J., Nordberg, R., Nordling, C., & Siegbanh, K. (1966). Electron Spectroscopy and Chemical Binding. *Nature, 210*, 4–8. doi:https://doi.org/10.1038/210004a0.
18. Grzibovskis, R., Vembris, A., Sebris, A., Kapilinskis, Z., & Turks, M. (2018). Energy Level Determination of Purine Containing Blue Light Emitting Organic Compounds. *Proc. SPIE., 10687*, 47. doi:10.1117/12.2307422.
19. Sworakowski, J., Lipiński, J., & Janus, K. (2016). On the Reliability of Determination of Energies of HOMO and LUMO Levels in Organic Semiconductors from Electrochemical Measurements. A Simple Picture Based on the Electrostatic Model. *Org. Electron., 33,* 300–310. doi:10.1016/j.orgel.2016.03.031.
20. Sworakowski, J., & Janus, K. (2017). On the Reliability of Determination of Energies of HOMO Levels in Organic Semiconducting Polymers from Electrochemical Measurements. *Org. Electron., 48,* 46–52. doi:10.1016/j.orgel.2017.05.031.
21. Whitcher, T.J., Wong, W.S., Talik, A.N., Woon, K.L., Rusydi, A., Chanlek, N., … & Songsiriritthigul, P. (2018). Energy Level Alignment of Blended Organic Semiconductors and Electrodes at the Interface. *Curr. Appl. Phys., 18,* 982–992. doi:10.1016/j.cap.2018.05.002.
22. Luo, H., Lai, J., Wang, C., & Chen, Q. (2018). Understanding the Effects of the Energy Band Alignment at the Donor/Acceptor Interface on the Open Circuit Voltage of Organic Photovoltaic Devices. *Chem. Phys. Lett., 711,* 113–117. doi:10.1016/j.cplett.2018.08.074.
23. Kim, H.B., & Kim, J.J. (2018). A Simple Method to Measure Intermolecular Charge-Transfer Absorption of Organic Films. *Org. Electron., 62*, 511–515. doi:10.1016/j.orgel.2018.06.022.
24. List, M., Sarkar, T., Perkhun, P., Ackermann, J., Luo, C., & Würfel, U. (2018). Correct Determination of Charge Transfer State Energy from Luminescence Spectra in Organic Solar Cells. *Nat. Commun., 9*, 1–8. doi:10.1038/s41467-018-05987-8.
25. Khan, S.U.Z., Londi, G., Liu, X., Fusella, M.A., D'Avino, G., Muccioli, L., … & Rand, B.P. (2019). Multiple Charge Transfer States in Donor-Acceptor Heterojunctions with Large Frontier Orbital Energy Offsets. *Chem. Mater., 31*, 6808–6817. doi:10.1021/acs.chemmater.9b01279.
26. Ruduss, A., Traskovskis, K., Grzibovskis, R., & Kokars, V. (2019). Synthesis and Photoelectrical Properties of 3-(Diphenylamino)Carbazolyl - Functionalized DMABI Derivatives. *Key Eng. Mater.,* 280–285. doi:10.4028/www.scientific.net/KEM.800.280.
27. Ruduss, A., Traskovskis, K., Vembris, A., Grzibovskis, R., Pudzs, K., Lielbardis, M., & Kokar, V. (2019). Synthesis and Investigation of Charge Transport Properties in Adducts of Hole Transporting Carbazole Derivatives and Push-Pull Azobenzenes. *J. Phys. Chem. Solids., 127*, 178–185. doi:10.1016/j.jpcs.2018.12.019.

sciendo

LATVIAN JOURNAL OF PHYSICS
AND TECHNICAL SCIENCES
2022, N 1

DOI: 10.2478/lpts-2022-0004

MORPHOLOGY INFLUENCE ON WETTABILITY AND WETTING DYNAMICS OF ZnO NANOSTRUCTURE ARRAYS

V. Gerbreders[1], M. Krasovska[1*], I. Mihailova[1], E. Sledevskis[1], A. Ogurcovs[1, 2],
E. Tamanis[1], V. Auksmuksts[1], A. Bulanovs[1], V. Mizers[1]

[1] G. Liberts' Innovative Microscopy Centre, Department of Technology,
Institute of Life Sciences and Technology, Daugavpils University,
1 Parades Str., Daugavpils, LV-5401, LATVIA
[2] Thin Films Laboratory, Institute of Solid State Physics,
University of Latvia, 8 Kengaraga Str., Riga, LV-1063, LATVIA
*e-mail: marina.krasovska@du.lv

Changes in nanostructure morphology and size may result in very different surface wettability. In this research, the impact of different morphological parameters on the wetting dynamics of ZnO nanostructured layers is studied. Six different morphologies are chosen to determine the specific wetting processes of ZnO nanostructures: nanoneedles, small diameter rods, large diameter rods, nanotubes, nanoplates, and plain thin films. Wetting dynamics is investigated using conventional sessile drop technique and a novel approach based on electrochemical impedance spectroscopy. The results show that the surface of nanostructured ZnO thin films exhibits both hydrophilic and hydrophobic wetting behaviour, depending on nanostructure form, size, and orientation. ZnO nanostructure arrays are a promising platform for electrochemical and optical sensing in aqueous solutions. The full and effective use of the sensor working surface can be ensured only under the condition of complete wetting of the nanostructured layer. Therefore, it is important to take into account the peculiarities of the wetting process of a specific morphology of nanostructures.

Keywords*: Electrochemical impedance spectroscopy, nanostructures, water contact angle, wettability, ZnO.*

1. INTRODUCTION

ZnO nanostructures have attracted considerable attention over the past few years because of noticeable properties coupled with efficient flexibility in morphology. These fascinating properties make them highly desirable for applications in chemisensors and biosensors, with good sensitivity and low detection limits for different analytes [1]–[4]. As it is well known, biosensors are instrumental analytical devices, which convert signals from molecular recognition elements into electrical or other types of signals, with the response being proportional to the target analyte concentration in the sample. ZnO nanostructures have large surface-to-volume ratios [5], [6] and, therefore, can deposit much larger amounts of bioanalytical materials on the nanostructures than on planar films, leading to an increase in signal intensity and sensitivity of the biosensor. Numerous methods for obtaining ZnO nanostructures, including gas phase [7] and solution phase methods [8], have led to the formation of structures with wurtzite lattices but different morphologies, which can be varied in diverse ways: by seed layers, acidity of growth solutions, various additives, or adjustment of other growth parameters [1], [9]. For sensor application, the optimal morphology is one that provides the maximum signal-to-noise ratio when examining the analyte under otherwise identical conditions. Therefore, achieving excellent sensitivity, selectivity, and reproducibility in analyte analysis is one of the main tasks in developing new and improved analytical methods.

Furthermore, electrochemical impedance spectroscopy (EIS) is an effective method for detecting physical, chemical, and biochemical changes in the environment [10]. This method is usable for manufacturing immunosensors [11], DNA sensors [12], glucose sensors [13], etc. When biomolecules (e.g., DNA, with an isoelectric point of 4.5) are deposited on ZnO nanostructures (isoelectric point of 9.5), interactions of the biomolecule-nanostructure electronic subsystems occur, changing the local potential. The process of biochemical reactions on ZnO nanostructures also leads to changes in electrical parameters, reflected in the frequency-dependent impedance of the system. Some authors argue that the change in resistance can be detected only at very small (about 20 mm) distances above the electrode surfaces, requiring the spacing between the electrodes to be reduced to a few microns [14]. However, in other works, a significant change in impedance is observed on sensors where the interval between two adjacent electrodes is about a millimetre [15]. In our opinion, sensor sensitivity is largely determined by the morphology of nanostructures that interact with the analyte, the general geometry of the device, and the specific processes that take place on the electrode, as shown in our previous article [1]. Withal, changes in morphology can alter wettabilities of pore surfaces. This phenomenon could be important in electrochemical sensor and biosensor applications.

The main focus of this study is to examine the influence of ZnO nanostructure morphologies on the wettability and sensitivity of sensors based on EIS. By the term “sensitivity,” we mean the value of the signal that is detected by the device resulting from processes occurring on the working surface. As a target substance, we choose distillate water, which does not chemically interact with ZnO; although, it can form structured monolayers at the ZnO-water interface [16],

[17]. Thereby, water, wetting the nanostructured ZnO films, penetrates the gaps between the nanostructures. Penetration rate depends on a number of factors, including shape, size, and density of nanostructures and surface conditions of ZnO, such as exposure to ultraviolet irradiation [18], [19]. Liquid penetration dynamics in the nanostructured film can be detected by EIS as the replacement of air in the voids by liquid must lead to a change in the impedance of the system. This phenomenon is useful in biosensors for wastewater monitoring. Furthermore, water can be used as a solvent for various biological solutions [20], [21]. In this case, biomolecules settle on the ZnO surface and change the wetting conditions of the nanostructures with water, altering the penetration dynamics of the liquid into nanostructure pores and, accordingly, changing the system impedance. Therefore, the concentration of biomolecules in the solution can be determined from the impedance change of the system. In addition, this method allows the saturation point (moment in time when the liquid completely fills air pockets of the nanostructured surface at the contact site) to be determined. In this paper, we describe the change in impedance of the system as a result of water penetration into depths of nanostructured films with different morphologies.

2. EXPERIMENTAL

2.1. Materials

Zinc nitrate hexahydrate ($Zn(NO_3)_2{\cdot}6H_2O$; ≥99.0 % CAS Number: 10196-18-6), zinc acetate ($Zn(CH_3COOH)_2{\cdot}2H_2O$; ≥99.0 %, CAS: 5970-45-6), hexamethylenetetramine ($C_6H_{12}N_4$; HMTA, ≥99.0 %, CAS Number: 100-97-0), and urea ($NH_2CONH_{2,}$ ≥99.0 %, CAS Number: 57-13-6) were purchased from Sigma Aldrich Co. All chemicals are analytical grade and used as received without further purification. Deionized and double-distilled water was self-made in the laboratory. Distilled water was purchased from Delfin Group.

2.2. Synthesis of ZnO Nanostructures

In this research, six different morphologies of ZnO nanostructures such as nanoneedles, small diameter rods (thin rods), large diameter rods (thick rods), nanotubes, plates and a plain thin film were selected for the study of the wetting processes. Standard microscope slides (76x26 mm) were used as samples substrates. First, 250 nm of chromium was deposited by DC magnetron sputtering through a patterned gate metal shadow mask onto pre-cleaned glass substrates by the LAB18 thin film deposition system (Kurt J. Lesker, USA). As a result, planar concentric Cr electrodes of 500 µm in width and 500 µm in spacing without galvanic contact were obtained (Fig. 1(6)). Secondly, the seed layer was prepared by coating Cr electrodes with zinc acetate solution in ethanol at 25 mmol concentration through the patterned shadow mask (made of metallic and rubber liners (gaskets), then washed with pure ethanol and dried in a nitrogen stream. The procedure was repeated three times and then samples were calcinated at 200 °C for 30 min and slowly cooled to room temperature.

Following seeding onto metalic electrodes ZnO nanostructures were grown by a hydrothermal method [22]. Generally for ZnO nanostructure synthesis zinc nitrate hexahydrate and hexamethylenetetramine aqueous solution are commonly used. Here, $Zn(NO_3)_2$ serves as a source of Zn^{2+} ions, water – a source for O^{2-} ions, and HMTA acts as a slowly decomposing weak base, which maintains the weakly alkaline environment in the solution and provides the desired amount of OH^- ions. A glass vessel with a lid was used as a chemical bath that was placed in a programmed Linn High Therm (Germany) oven preheated to 90 °C. The ZnO seeded substrates were placed at an angle against the vessel, with the seed layer facing down. Depending upon the concentration of the reactants and the temperature of growth, the formation of ZnO nanostructures with different morphology was observed.

Thick rods: ZnO nanorod arrays were synthesized in 0.1M equimolar aqueous solution of zinc nitrate hexahydrate and HMTA at 90 °C for 3h.

Thin rods: For obtaining thin rods 0.05M Zn $(NO_3)_2$ + 0.2M HMTA solution were used. The growth process was carried out at 90 °C for 3h.

Tubes: ZnO nanotubes were obtained by using a self-selective etching method with lowering temperatures of growth during the hydrothermal process. This method is based on pH level change after a decrease in growth temperature [23]–[27]. For the experiment 0.2M equimolar $Zn(NO_3)_2$ and HMTA concentration were used. At the first stage, in relatively short time (3h) at 90 °C temperature the growth process of ZnO nanorods intensively occurs in both lateral and axial directions. At the second stage at 50 °C in a significantly longer time period, compared to the first stage (18 h), the aging process occurs: ZnO metastable planes are etched with residual chemicals of growth solution.

Needles: As indicated above, the main role of HMTA is to provide OH- ions; therefore, it was hypothesized that increasing the HMTA concentration in growth solution would cause the pH increase without the use of an additional chemical, like ammonia or hydroxides. ZnO nanoneedles arrays were synthesized in 0.05M Zn $(NO_3)_2$ + 0.2M HMTA solution at 90 °C for 3h.

Plates: This morphology was obtained by replacing HMTA with urea, which promoted lateral growth and inhibited growth in the axial (c-axis) direction during the hydrothermal synthesis process. As a result, the total surface area of (0002) planes increased, but the lateral surface area decreased. 2D plate-like ZnO nanostructures were grown in aqueous solution of 30 mM zinc nitrate and 0.5M urea at 90 °C for 3h. After hydrothermal growth samples were annealed at 250°C for 2h, in order to calcine the obtained zinc carbonate to ZnO.

After hydrothermal growth, all obtained samples were thoroughly washed with distilled water in order to remove traces of the growth solution from the surface of nanostructures. Then, the samples were dried in oven for one hour at a temperature of 90°C in order to get rid of residual water accumulated on their surface and in the space between the nanostructures.

The unstructured 150 nm thick **ZnO film** was obtained by magnetron sputtering (MS) mode in Kurt J. Lesker LAB 18 sputtering system.

2.3. Characterization

The surface morphology and structural properties were studied using a scanning electron microscopy (SEM, TESCAN-VEGA LMU II operated at 30kV).

Surface wettability of obtained ZnO thin films was identified by measuring the water contact angle (WCA) at ambient temperature using the sessile drop method by an optical microscope (Motic BA50-X). A 3 µL droplet of distilled water was placed on the sample surface, and digital images of the droplet silhouette were captured with the implemented camera every minute for 10 minutes. The WCA was determined using the Motic Images Plus image processing software. An average of five measurements, performed at different spots on the same sample, was adopted as the WCA. Surface roughness and surface coverage of nanostructures were analysed with ImageJ Analysis software.

Additional experiments were carried out to determine the impact of surface morphology on the wetting dynamics by EIS. Electrochemical measurements were performed at room temperature with a VersaSTAT 3 (Princeton Applied Research) potentiostat/galvanostat. Structures of the electrical measurement cell and electrodes are shown in Fig. 1. ZnO-coated Cr electrodes were used as the counter and working electrodes. A drop of the target liquid (250 µl) was pelleted on the cell with the electrodes, and the dependence of the phase shift on frequency was measured immediately and repeated every minute for 10 minutes. An average of eight independent measurements, performed at different spots on the same sample, was adopted to establish dependency between wetting dynamics and surface structure of all ZnO nanostructure morphologies.

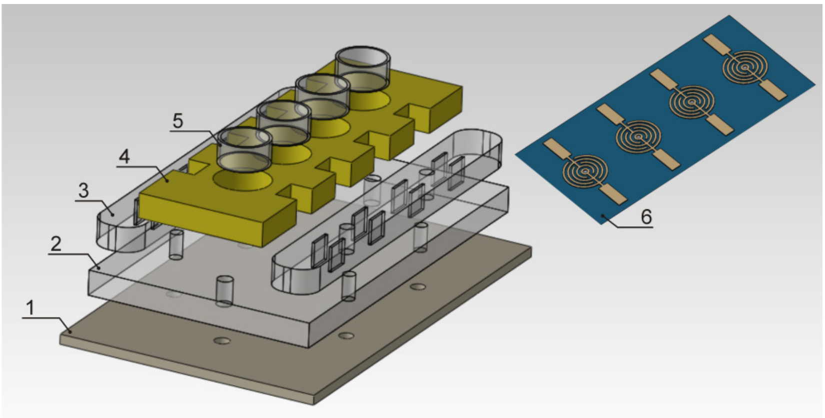

Fig. 1. Structure of the electrical measurement cell (left) and electrodes (right). The measurement cell consists of the following parts: a corps (1), an interlayer (2) with push-in contacts (3), a sealing rubber mask (4) with replaceable plastic cylinders (5). Sample (6) consists of four electrodes, which allow four independent analyte measurements to be performed consistently [1].

3. RESULTS AND DISCUSSION

3.1. Wettability versus Surface Morphology

Surface morphologies of the prepared samples were characterised using SEM. Figure 2 demonstrates six different types of ZnO nanostructures: nanoneedles (Fig. 2a), small diameter rods (Fig. 2b), large diameter rods (Fig. 2c), nanotubes (Fig. 2d), plates

(Fig. 2e), and a thin 150 nm MS layer (Fig. 2f). As seen in Fig. 2, the nanoneedle array was not aligned. The average diameter of the base stems and their heads were around 350 and 60 nm, respectively. The average length of the ZnO nanoneedle stems was around 1 μm. ZnO nanorod arrays and nanotubes with hexagonal structures were preferentially oriented towards the c-axis perpendicular to the glass substrate. The smaller nanorods had an average diameter of ~100 nm, while larger nanorods and nanotubes were around 1 μm. The ZnO nanoplates were very dense, with thicknesses of approximately 300 nm. The nanoscale roughness on the film surfaces reduced the contact area between the solid and droplet; thereby, a large amount of air was entrapped into the space below the droplet, effecting the wettability of the surface.

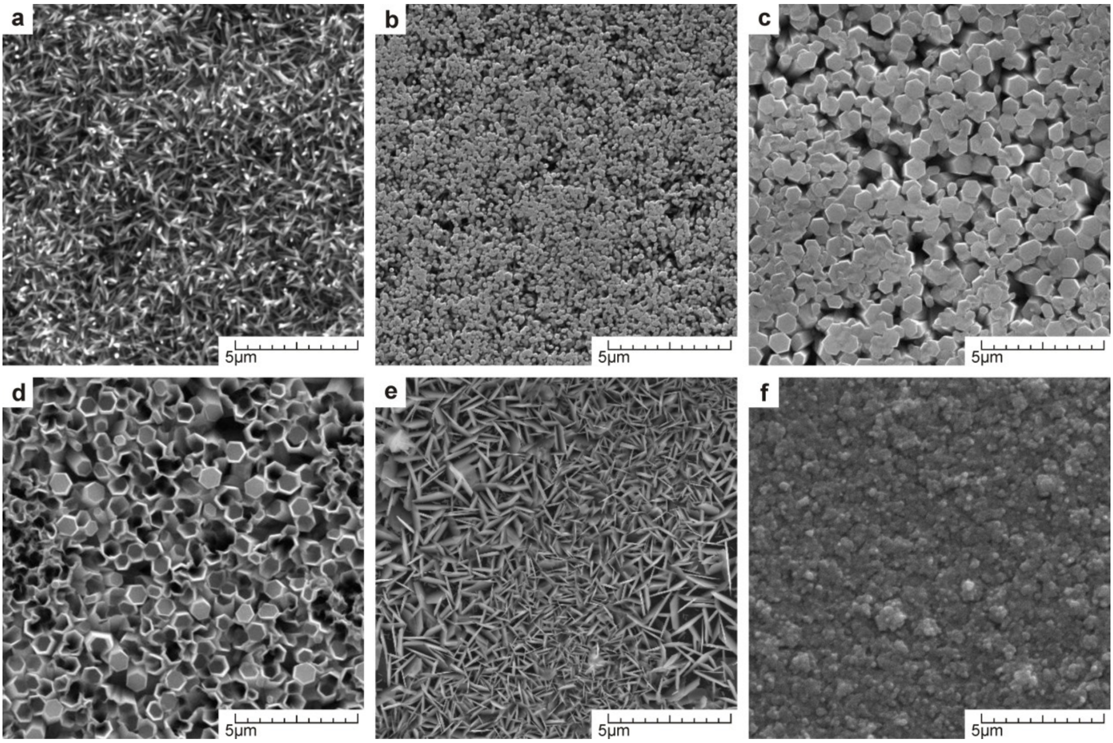

Fig. 2. Morphology of ZnO thin films: **(a)** nanoneedles, **(b)** thin rods, **(c)** thick rods, **(d)** nanotubes, **(e)** nanoplates, and **(f)** the MS thin film.

Myo Tay Zar Myint et al. point out that for homogeneous, unstructured, and untreated ZnO thin films, consisting of many chaotically oriented nanocrystallites, the intrinsic WCA is 26±3° [28]–[31]. Some other articles refer to different WCA values, which are, in general, smaller than 50°, indicating the hydrophilic nature of the ZnO surface [32]. However, in the case of nanostructured ZnO thin films, the surface can exhibit both hydrophobic and hydrophilic behaviour depending on the nanostructure parameters, and the transition from hydrophilic to hydrophobic conditions can be realised by micro- and nanostructuring of the surface [33]–[38].

In our opinion, there are two main factors that determine the wettability of an individual sample: the surface coverage of the nanostructures (percentage ratio of the solid phase and voids) and the nanostructure morphologies, which determine the number of active sites capable of binding hydroxyl groups. The first hypothesis has also been proven in previous work [28], which indicates the possibility of changing the wettability of the ZnO surface by micro/nanostructuring [39]. As mentioned in the article, surfaces with nanostructure coverage areas less than 39 % show hydrophobic character, and the classical Cassie–Baxter criteria can be applied to the so-called "Fakir" surface (Fig. 3a) [28], [40]. However, for high solid area fractions (>40 %), the surface was completely wet, and water penetrated into the pores. In such a case, Wenzel gave a wettability description of the films (Fig. 3b).

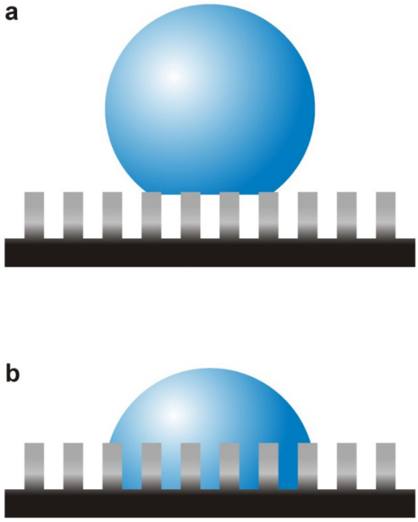

Fig. 3. Schematic illustration of (a) Cassie–Baxter and (b) Wenzel regimes.

These hypotheses have also been confirmed in our experiment, where samples are represented by several rod-type nanostructures that differ in size and, respectively, in the degree of surface coverage (Figs. 2a–d). Figure 4 shows the dependence of the wetting angle on the time for each morphology. The highest WCA value was observed for ZnO nanoneedle (Fig. 2a) arrays: 127° at the beginning of the measurement and 70° after 10 minutes (Fig. 4, red curve). The surface structure of this sample can be characterised by the lowest degree of surface coverage (23 %). The hydrophobic effect was also enhanced by the existence of the 'fakir' or 'lotus' surfaces, when the interaction between the droplets and solid surface was reduced to the point contact because of the needle-like nanostructure shapes. In the case of thin rod shaped nanostructures (Fig. 2b), an increase in surface coverage to 38 % was observed, promoting a decrease in a wetting angle and total omission of the graph for angle-time dependence indicating a decrease in hydrophobic properties compared to nanoneedles. The value of the wetting angle changed from 86° to 57° within 10 minutes (Fig. 4, blue curve). The decrease in the initial WCA value compared to nanoneedles may be explained by the increase in contact surface due to the flat top of the nanorods, leading to a stronger interaction between the water and solid surface. In the case of thick rods (Fig. 2c), the surface coverage increased up to 87 %. Therefore, in contrast with previous rod-shaped morphologies, hydrophilic surface behaviour was observable; the wetting angle did not exceed 19° at the starting point or 7.5° after 10 minutes (Fig. 4, green curve). In the case of the MS thin film (Fig. 2f), the WCA was 44° at the starting point and remained almost constant over time (Fig. 4, black line). Minor changes may have been caused by slight spreading of the droplet on the surface.

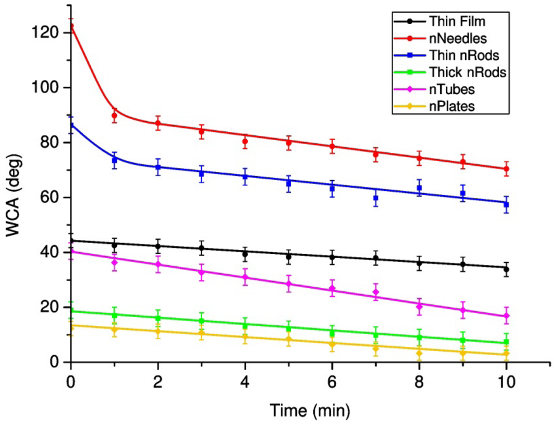

Fig. 4. WCA changes over time for different ZnO nanostructure morphologies.

Comparing large diameter nanorod and MS thin film wetting angle values, a difference of 30° was observed for the starting point of the wetting angle with only a very small surface coverage difference between the two samples (≈10 %). This difference indicates a stronger interaction between the liquid and solid surface for the nanostructured sample. Importantly, the surface coverage is influential but is not the only factor that determines surface wetting; nanostructure morphology also accounts for significant contributions. As it is known, ZnO nanostructures have the form of a hexagonal prism, in which the two most significant plane groups can be distinguished. The first group includes nonpolar side {1010} planes, containing both zinc ions and oxygen and being electrically neutral and chemically stable. The second group includes metastable polar {0001} planes, consisting of either oxygen ions or zinc ions (Zn-terminated or O-terminated planes), which have an electric charge and are chemically more active. The structure of the MS thin film can be described as a set of randomly oriented crystallites. Meanwhile, the nanorod array (nanostructured sample) is compositionally arranged and, in a horizontal plane, is represented by a metastable plane [0002], containing a large number of active adsorption bonds on its surface. An important role of this plane was also confirmed by WCA measurements of ZnO nanoplate arrays, for which, considering the preferential growth direction, this plane was dominant. This morphology showed the hydrophilic behaviour and even smaller contact angle values than in the previous case: 12º at the beginning of the experiment and 3º after 10 minutes (Fig. 4, yellow curve). This indicates that both coverage and nanostructure morphology play an important role.

In particular, the ZnO nanotube morphology (Fig. 2d) deserves special attention. Despite the low percentage of surface coverage by these nanostructures (40 %), as well as a decreased total area of the [0002] plane, this morphology revealed strongly hydrophilic behaviour: 40º at the beginning of process and 17º after 10 minutes (Fig. 4, pink curve). This phenomenon could be explained by the presence of a large number of active adsorption centres that are related to structure defects formed on the inner walls of nanotubes during the etching process. Such centres have higher adsorption energy values compared to non-polar centres and provide stronger interaction between water and solid.

3.2. Analysis of the Wetting Process by EIS

The aim of this study is to describe the usage of EIS as an alternative method for analysing the wetting processes of nanostructured surfaces. This technique makes it possible to describe, with great accuracy, the wetting processes, not only on the surface, but also in the volume of the nanostructured layer due to changes in the sample resistance in the process of filling the pores with liquid. Furthermore, this method allows us to track dynamics of the wetting process for each morphology, as well as determine the saturation time, i.e., the moment in time where complete wetting of all structures occurs. Also, this method allows us to describe the dynamics of intermediate processes that occur during wetting and the transition from the Cassie-Baxter model at the beginning of the process to the Wenzel model at the end, when all nanostructure voids are completely filled with water.

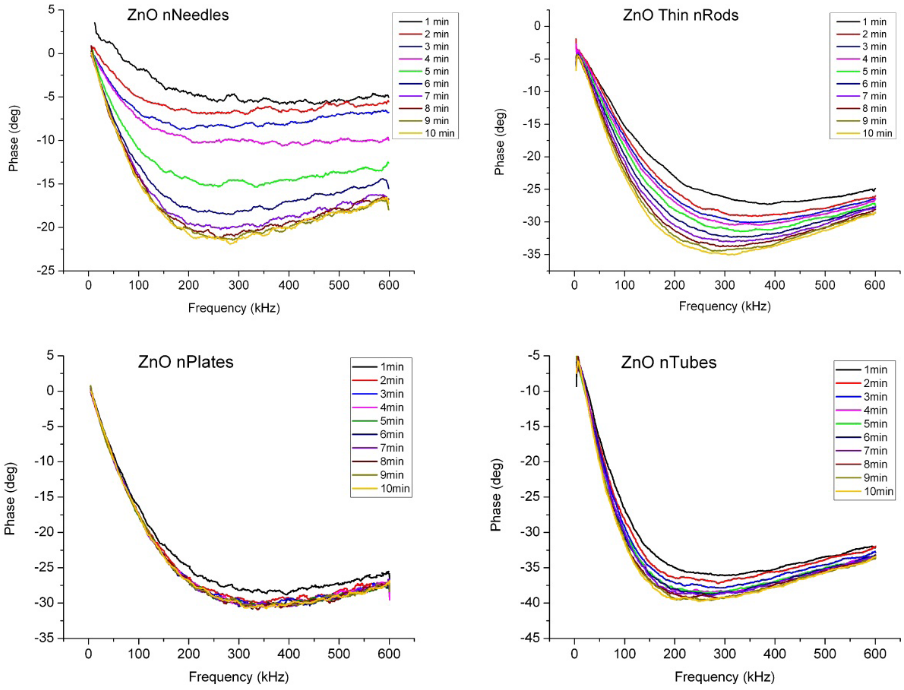

Fig. 5. EIS spectra for the wetting process for different ZnO nanostructure morphologies.

Figure 5 shows the phase dependence curves over time for two hydrophobic (upper row) and two hydrophilic (bottom row) ZnO nanostructure morphologies. As can be seen, the wetting process is uneven and non-linear. In the first few minutes, there is a large difference between the phases of adjacent curves. However, over time, this step decreases until the phase difference becomes minimal, and the curves coincide. This moment can be defined as the moment of saturation, which characterises complete wetting of the nanostructured sample. As expected, in the case of hydrophobic surfaces, the dynamics of phase change is more readily expressed, and the saturation state is characterised by a longer time interval (7–9 minutes). In the case of hydrophilic surfaces, the saturation occurs much faster (2–4 minutes), and the phase value changes are smaller.

To better understand the degree of hydrophobicity of the structures, the graph of the relative change in impedance versus time is very descriptive (Fig. 6). This curve characterises the change in impedance of the full system relative to the zero point, which corresponds to the beginning of the measurements and characterises the amount of liquid absorbed by the entire volume of the nanostructured sample. In the case of the plain film, the relative changes in impedance are minimal and occur only due to absorption of liquid by small irregularities arising from the polycrystalline structure of the sample. For large diameter rods, the relative changes in impedance are caused by the penetration of water into the voids between nanostructures. However, as the oriented nanorods are dense and the voids are narrow, the dynamics is poorly expressed. In the case of nanoplates, there is a slight increase in relative impedance changes over time. The relative changes in impedance do not exceed 12 % and the rapid wetting is caused by both a decrease of surface coverage (increase in porosity) and an increase in the total area of the metastable [002] plane. At the beginning of the measurement, voids are almost completely filled with water, so in case of hydrophilic nanostructures further impedance values practically do not change over time. For nanotubes, the wetting process is significantly slower than for nanoplates and thick rods and is mainly provided by cavities in the nanostructures reducing the degree of surface filling compared with the same diameter nanorods. However, the morphology still shows hydrophilic properties due to the presence of a large number of structural defects formed on the inner walls during etching process which prevent the manifestation of completely hydrophobic properties. This fact shows good conformity with theory and WCA measurements described in Section 3.1. For small diameter nanorods and nanoneedles, the relative increase in impedance is caused by a decrease in the surface coverage, correlating well with WCA measurements (Fig. 4).

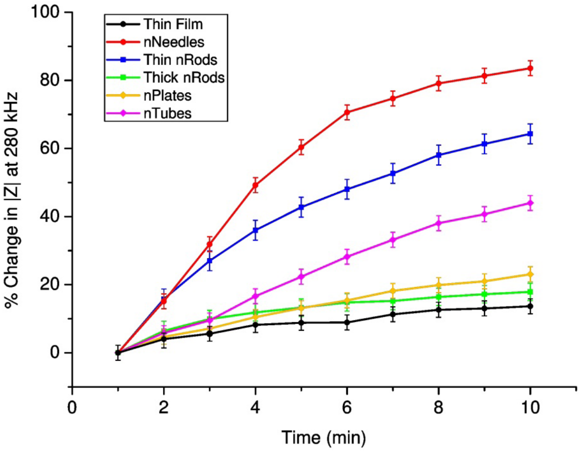

Fig. 6. Relative change (in %) of the impendance module |Z| versus time for different ZnO nanostructure morphologies (as indicated in the legend) at 280 kHz.

4. CONCLUSION

The surface of nanostructured ZnO thin films exhibits both hydrophilic and hydrophobic wetting behaviour, depending on nanostructure form, size, and orientation. ZnO nanoneedles with WCAs of 127º at the beginning of the experiment, as well as thin nanorods with WCAs of 86º, are hydrophobic. In contrast, ZnO thin film (44º), thick nanorods (19º), nanoplates (12º), and nanotubes (40º) exhibit hydrophilic behaviour.

We have demonstrated the possibility of investigate wetting processes by EIS. With great accuracy, this technique describes both surface wetting and processes occurring at the volume of the nanostructured layer. Thus, this method allows us to describe dynamics of the wetting process when the Cassie-Baxter wetting model at the beginning of the process is gradually replaced with a Vensel model at the end of the process, thus facilitating the determination of the saturation value (moment in time when liquid completely fills air pockets of the nanostructured surface). In cases of hydrophobic behaviour, saturation occurs within 7–9 minutes, but hydrophilic morphologies are fully wetted within 2–4 minutes.

The results obtained by EIS correspond to the results obtained by the optical method.

ACKNOWLEDGEMENTS

This study has been supported by internal research grant No. 14-95/2021/10 of Daugavpils University "Development of the Nanostructured Metal Oxide Coatings and Their Application in Optical Sensing for Heavy Metal Detection".

REFERENCES

1. Krasovska, M., Gerbreders, V., Mihailova, I., Ogurcovs, A., Sledevskis, E., Gerbreders, A., & Sarajevs, P. (2018). ZnO-Nanostructure-Based Electrochemical Sensor: Effect of Nanostructure Morphology on the Sensing of Heavy Metal Ions. *Beilstein Journal of Nanotechnology*, *9*, 2421–2431. DOI:10.3762/bjnano.9.227.
2. Tereshchenko, A., Bechelany, M., Viter, R., Khranovskyy, V., Smyntyna, V., Starodub, N., & Yakimova, R. (2016). Optical Biosensors Based on ZnO Nanostructures: Advantages and Perspectives. A Review. *Sensors and Actuators B: Chemical, 229,* 664–677. DOI:10.1016/j.snb.2016.01.099.
3. Zaidi, S. A., & Shin, J. H. (2016). Recent Developments in Nanostructure Based Electrochemical Glucose Sensors. *Talanta, 149,* 30–42. DOI:10.1016/j.talanta.2015.11.033.
4. Arya, S. K., Saha, S., Ramirez-Vick, J. E., Gupta, V., Bhansali, S., & Singh, S. P. (2012). Recent Advances in ZnO Nanostructures and Thin Films for Biosensor Applications: Review. *Analytica Chimica Acta, 737,* 1–21. DOI:10.1016/j.aca.2012.05.048.
5. Mihailova, I., Gerbreders, V., Tamanis, E., Sledevskis, E., Viter, R., & Sarajevs, P. (2013). Synthesis of ZnO Nanoneedles by Thermal Oxidation of Zn Thin Films. *Journal of Non-Crystalline Solids, 377,* 212–216. DOI:10.1016/j.jnoncrysol.2013.05.003.

6. Mihailova, I., Gerbreders, V., Bulanovs, A., Tamanis, E., Sledevskis, E., Ogurcovs, A., & Sarajevs, P. (2014). Controlled growth of well-aligned ZnO nanorod arrays by hydrothermal method. In: *Eighth International Conference on Advanced Optical Materials and Devices,* (pp. 1–8), 25–27 August 2014, 9421, 94210A. Riga, Latvia: SPIE. DOI:10.1117/12.2083960.
7. Alvi, N. H., Hassan, W. ul, Farooq, B., Nur, O., & Willander, M. (2013). Influence of Different Growth Environments on the Luminescence Properties of ZnO Nanorods Grown by the Vapor–Liquid–Solid (VLS) Method. *Materials Letters, 106*, 158–16. DOI:10.1016/j.matlet.2013.04.074.
8. Abbas, K. N., Bidin, N., Sabry, R. S., Al-Asedy, H. J., Al-Azawi, M. A., & Islam, S. (2016). Structures and Emission Features of High-Density ZnO Micro/Nanostructure Grown by an Easy Hydrothermal Method. *Materials Chemistry and Physics, 182,* 298–307.DOI:10.1016/j.matchemphys.2016.07.035.
9. Baruah, S., & Dutta, J. (2009). Hydrothermal Growth of ZnO Nanostructures. *Science and Technology of Advanced Materials, 10* (1), 013001. DOI:10.1088/1468-6996/10/1/013001.
10. Katz, E., & Willner, I. (2003). Probing Biomolecular Interactions at Conductive and Semiconductive Surfaces by Impedance Spectroscopy: Routes to Impedimetric Immunosensors, DNA-Sensors, and Enzyme Biosensors. *Electroanalysis, 15* (11), 913–947. DOI:10.1002/elan.200390114.
11. Lin, D., Tang, T., Jed Harrison, D., Lee, W. E., & Jemere, A. B. (2015). A Regenerating Ultrasensitive Electrochemical Impedance Immunosensor for the Detection of Adenovirus. *Biosensors and Bioelectronics, 68,* 129–134. DOI:10.1016/j.bios.2014.12.032.
12. Kafka, J., Pänke, O., Abendroth, B., & Lisdat, F. (2008). A Label-Free DNA Sensor Based on Impedance Spectroscopy. *Electrochimica Acta, 53* (25), 7467–7474. DOI:10.1016/j.electacta.2008.01.031.
13. Ni, Y., Xu, J., Liang, Q., & Shao, S. (2017). Enzyme-Free Glucose Sensor Based on Heteroatom-Enriched Activated Carbon (HAC) Decorated with Hedgehog-Like NiO Nanostructures. *Sensors and Actuators B: Chemical, 250,* 491–498. DOI:10.1016/j.snb.2017.05.004.
14. Sanguino, P., Monteiro, T., Bhattacharyya, S. R., Dias, C. J., Igreja, R., & Franco, R. (2014). ZnO Nanorods as Immobilization Layers for Interdigitated Capacitive Immunosensors. *Sensors and Actuators B: Chemical, 204,* 211–217. doi:10.1016/j.snb.2014.06.141.
15. Jacobs, M., Muthukumar, S., Munje, R., Quadri, B., & Prasad, S. (2014). Analysis of nanotextured ZnO surfaces for biosensing applications. In: *14th IEEE International Conference on Nanotechnology*, (pp. 515–520), 18–21 August 2014. Toronto, Canada: IEEE. DOI:10.1109/nano.2014.6968149.
16. Raymand, D., van Duin, A. C. T., Spångberg, D., Goddard, W. A., & Hermansson, K. (2010). Water Adsorption on Stepped ZnO Surfaces from MD Simulation. *Surface Science, 604* (9–10)*,* 741–752. DOI:10.1016/j.susc.2009.12.012.
17. Hamid, S. B. A., Teh, S. J., & Lai, C. W. (2017). Photocatalytic Water Oxidation on ZnO: A Review. *Catalysts, 7* (12)*,* 93. DOI:10.3390/catal7030093.
18. Bhavsar, K., Ross, D., Prabhu, R., & Pollard, P. (2015). LED-Controlled Tuning of ZnO Nanowires' Wettability for Biosensing Applications. *Nano Reviews, 6* (1)*,* 26711. DOI:10.3402/nano.v6.26711.
19. Khranovskyy, V., Ekblad, T., Yakimova, R., & Hultman, L. (2012). Surface Morphology Effects on the Light-Controlled Wettability of ZnO Nanostructures. *Applied Surface Science, 258* (20), 8146–8152. DOI:10.1016/j.apsusc.2012.05.011.
20. Ejeian, F., Etedali, P., Mansouri-Tehrani, H.-A., Soozanipour, A., Low, Z.-X., Asadnia, M., …. & Razmjou, A. (2018). Biosensors for Wastewater Monitoring: A Review. *Biosensors and Bioelectronics, 118,* 66–79. DOI:10.1016/j.bios.2018.07.019.
21. Duta, L., Popescu, A. C., Zgura, I., Preda, N., & Mihailescu, I. N. (2015). Wettability of Nanostructured Surfaces. *Wetting and Wettability,* Intech Open*,* 207–252. DOI:10.5772/60808.

22. Krasovska, M., Gerbreders, V., Sledevskis, E., Gerbreders, A., Mihailova, I., Tamanis, E., & Ogurcovs, A. (2020). Hydrothermal Synthesis of ZnO Nanostructures with Controllable Morphology Change. *CrystEngComm., 28* (8), 1346–1358. DOI:10.1039/c9ce01556f.
23. Krasovska, M., Gerbreders, V., Paskevics, V., Ogurcovs, A., & Mihailova, I. (2015). Obtaining a Well-Aligned ZnO Nanotube Array Using the Hydrothermal Growth Method. *Latvian Journal of Physics and Technical Sciences, 52* (5), 28–40. DOI:10.1515/lpts-2015-0026.
24. Gerbreders, V., Krasovska, M., Mihailova, I., Ogurcovs, A., Sledevskis, E., Gerbreders, A., … & Plaksenkova, I. (2019). ZnO Nanostructure-Based Electrochemical Biosensor for Trichinella DNA Detection. *Sensing and Bio-Sensing Research, 100276.* DOI:10.1016/j.sbsr.2019.100276.
25. Chae, K.-W., Zhang, Q., Kim, J. S., Jeong, Y.-H., & Cao, G. (2010). Low-Temperature Solution Growth of ZnO Nanotube Arrays. *Beilstein Journal of Nanotechnology, 1,* 128–134. DOI:10.3762/bjnano.1.15.
26. Roza, L., Rahman, M. Y. A., Umar, A. A., & Salleh, M. M. (2015). Direct Growth of Oriented ZnO Nanotubes by Self-Selective Etching at Lower Temperature for Photo-Electrochemical (PEC) Solar Cell Application. *Journal of Alloys and Compounds, 618,* 153–158. DOI:10.1016/j.jallcom.2014.08.113.
27. Wang, H., Li, G., Jia, L., Wang, G., & Tang, C. (2008). Controllable Preferential-Etching Synthesis and Photocatalytic Activity of Porous ZnO Nanotubes. *The Journal of Physical Chemistry C, 112(31),* 11738–11743. DOI:10.1021/jp803059k.
28. Myint, M. T. Z., Kumar, N. S., Hornyak, G. L., & Dutta, J. (2013). Hydrophobic/Hydrophilic Switching on Zinc Oxide Micro-Textured Surface. *Applied Surface Science, 264,* 344–348. DOI:10.1016/j.apsusc.2012.10.024.
29. Patel, K. H., & Rawal, S. K. (2016). Exploration of Wettability and Optical Aspects of ZnO Nano Thin Films Synthesized by Radio Frequency Magnetron Sputtering. *Nanomaterials and Nanotechnology, 6,* 22. DOI:10.5772/62804.
30. Han, J., & Gao, W. (2008). Surface Wettability of Nanostructured Zinc Oxide Films. *Journal of Electronic Materials, 38* (4), 601–608. DOI:10.1007/s11664-008-0615-0.
31. Shaban, M., Zayed, M., & Hamdy, H. (2017). Nanostructured ZnO Thin Films for Self-Cleaning Applications. *RSC Advances, 7* (2), 617–631. DOI:10.1039/c6ra24788a.
32. Lin, L.-Y., Kim, H.-J., & Kim, D.-E. (2008). Wetting Characteristics of ZnO Smooth Film and Nanowire Structure with and without OTS Coating. *Applied Surface Science, 254* (22), 7370–7376. DOI:10.1016/j.apsusc.2008.05.337.
33. Subedi, D. P., Madhup, D. K., Sharma, A., Joshi, U. M., & Huczko, A. (2012). Retracted: Study of the Wettability of ZnO Nanofilms. *International Nano Letters, 2* (1), 117–122. DOI:10.1186/2228-5326-2-1.
34. Mao-Gang, G., Xiao-Liang, X., Zhou, Y., Yan-Song, L., & Ling, L. (2010). Superhydrophobic Surfaces via Controlling the Morphology of ZnO Micro/Nano Complex Structure. *Chinese Physics B, 19* (5), 056701. DOI:10.1088/1674-1056/19/5/056701.
35. Yang, P., Wang, K., Liang, Z., Mai, W., Wang, C., Xie, W., … & Song, J. (2012). Enhanced Wettability Performance of Ultrathin ZnO Nanotubes by Coupling Morphology and Size Effects. *Nanoscale, 4* (18), 5755. DOI:10.1039/c2nr31380d.
36. Suresh Kumar, P., Sundaramurthy, J., Mangalaraj, D., Nataraj, D., Rajarathnam, D., & Srinivasan, M. P. (2011). Enhanced Super-Hydrophobic and Switching Behavior of ZnO Nanostructured Surfaces Prepared by Simple Solution – Immersion Successive Ionic Layer Adsorption and Reaction Process. *Journal of Colloid and Interface Science, 363* (1), 51–58. DOI:10.1016/j.jcis.2011.07.015.
37. Piech, M., Sounart, T. L., & Liu, J. (2008). Influence of Surface Morphology on the Wettability of Microstructured ZnO-Based Surfaces. *The Journal of Physical Chemistry C, 112* (51), 20398–20405. DOI:10.1021/jp804815x.

38. Zhou, X., Guo, X., Ding, W., & Chen, Y. (2008). Superhydrophobic or Superhydrophilic Surfaces Regulated by Micro-Nano Structured ZnO Powders. *Applied Surface Science, 255* (5), 3371–3374. DOI:10.1016/j.apsusc.2008.09.080.
39. Ennaceri, H., Wang, L., Erfurt, D., Riedel, W., Mangalgiri, G., Khaldoun, A., … & Ennaoui, A. (2016). Water-Resistant Surfaces Using Zinc Oxide Structured Nanorod Arrays with Switchable Wetting Property. *Surface and Coatings Technology, 299,* 169–176. DOI:10.1016/j.surfcoat.2016.04.056.
40. Singh, A., & Singh, S. (2018). ZnO Nanowire-Coated Hydrophobic Surfaces for Various Biomedical Applications. *Bulletin of Materials Science, 41(4)*. DOI:10.1007/s12034-018-1611-5.

LATVIAN JOURNAL OF PHYSICS
AND TECHNICAL SCIENCES
2022, N 1

DOI: 10.2478/lpts-2022-0005

INVESTIGATION OF POWER EFFICIENCY CHANGES IN DWDM SYSTEMS REPLACING ERBIUM-DOPED AMPLIFIERS BY SEMICONDUCTOR OPTICAL AMPLIFIERS

D. Pavlovs*, V. Bobrovs, M. Parfjonovs,
A. Alsevska, G. Ivanovs

Riga Technical University,
Institute of Telecommunications,
12 Azenes Str., Riga, LV-1048, LATVIA
*e-mail: deniss.pavlovs_5@edu.rtu.lv

To evaluate potential utilization of semiconductor optical amplifiers (SOAs) as a wide-band amplification alternative to erbium doped fibre amplifiers (EDFAs) in dense wavelength division multiplexed (DWDM) coherent systems, the authors discuss changes in power consumption levels required for a single bit transmission. The research evaluates the power efficiency parameter for WDM transmission systems using both amplification schemes – EDFAs that utilise standard C-band and SOAs assuming 75 nm amplification spectral band. The power efficiency levels have been estimated for five transmission spans with maximal distance of 640 km. The standard 50 GHz channel spacing has been chosen for both system configurations to allocate 100 Gbps dual-polarization quadrature phase shift keying (DP-QPSK) optical signals. The simulation schemes are described along with the critical parameters, derived from the recent relevant studies that should be taken into account considering usage of SOAs as in-line amplifiers.

Keywords: *Coherent SOA-amplified transmission systems, DWDM systems, phase modulation formats, power efficiency, semiconductor optical amplifier, SOA as in-line amplifiers*.

1. INTRODUCTION

To fulfil continuous Internet and mobile traffic demand that is dictated by a globally growing number of internet users, high-dense applications, connected devices to the IP networks and machine-to-machine (M2M) connections, such as the Internet of Things (IoT) [1], several advanced techniques have been proposed in recent years to increase spectral efficiency and capacity of coherent multi-span wavelength division multiplexed (WDM) transmission systems. Among others, these include high cardinality shaped constellations, single-channel digital nonlinear compensation, and adaptive-rate capacity approaching forward error correction codes [2]–[4]. On the other hand, maximization of the spectral efficiency and capacity is tightly linked with the system energy consumption due to the necessity to maintain a specific quality of transmission (QoT) level for proper system functioning. The combination of these two factors defines a constant trade-off between efficient utilization of an available bandwidth and power required for a signal transmission through the optical fibre link, which raises ecological concerns for operators, such as carbon footprint produced by the entire sector of information and communication technologies (ICT), which is ~1.4 % of overall global emissions [5].

The total capacity per single-mode fibre span fundamentally is limited by the physical properties of the optical fibre, such as fibre losses, Kerr nonlinear coefficient, and dispersion coefficients, and by the optical amplifier bandwidth and noise figure (NF) parameters. This has determined the high potential of EDFA utilization as in-line optical amplifiers due to its relatively low NF and amplification bandwidth, which correlates with the lowest fibre losses within optical C-band. Nevertheless, the limited capacity of C-band cannot fulfil continuously growing traffic demand in core networks since current technologies will soon reach the limits set by the information theory and the physics of optical signal propagation through the optical fibre [6]. In the past decade, in order to extend total throughput, several solutions were designed to combine C and L spectral bands for WDM transmission systems. Recent studies have evaluated the C+L EDFAs [3], [7] and Raman amplification [8] providing optical bandwidth about 9 THz, but these methods still have their deficiencies, such as Raman amplifier distributed amplification and higher energy consumption. The above-mentioned traffic demand increment and existing system drawbacks have stimulated studies devoted to the examination of SOA as a more integrated and low-cost alternative. It has been demonstrated that SOA amplification bandwidth can reach up to 120 nm [9]. Also, the nonlinear impairments of SOAs can be reduced by different time variations of the optical signal envelope due to the present use of combined amplitude and phase modulation formats and dispersion unmanaged fibre spans. In 2017 and 2018, the specific WDM system design was demonstrated, which used custom designed in-line ultra-wideband SOAs with about 100 nm continuous optical amplification band [10], [11]. Additionally, the numerical investigation [12] was performed and the theoretical model [13] of SOAs as in-line optical amplifiers was developed, which provided useful guidelines for parameter definition for the current study and motivation to reconsider SOAs for in-line amplification techniques within DWDM systems in terms of higher power efficiency, low costs and wide amplification range.

2. EXPERIMENTAL

The information collection and processing methodology remains similar and has been described in more detail in previous studies [14], [15]. Only input data and system parameters have been changed in accordance with the aims of the present research. Therefore, we devote more attention to parameter definition rationale. At the first step, we simulated DWDM transmission links with EDFA and SOA amplifications for several transmission lengths using the RSoft OptSim Sample-mode environment, WDM component datasheets and outcomes of recent studies with regard to specific SOA parameter definitions. The designed transmission system does not incorporate FEC (forward error correction) schemes; therefore, the main aim of this step was to reach Q factor level higher than 16 dB at a receiver, which corresponded to 10^{-9} bit error ratio (BER), which was measured at the most degraded channel – central channel. By reaching the required Q levels for a different number of fibre spans, during the next step the analytical model was created in Matlab environment for the power consumption, system capacity and power efficiency calculations, defining power consumption values from available WDM component datasheets.

To simulate optical signal propagation through the DWDM fibre link with different amplification techniques, we composed nine transmission channels spaced (*Δf*) by 50 GHz and utilising 100 Gbps dual-polarization quadrature phase shift keying (DP-QPSK) modulation. Simplified system design is shown in Fig. 1.

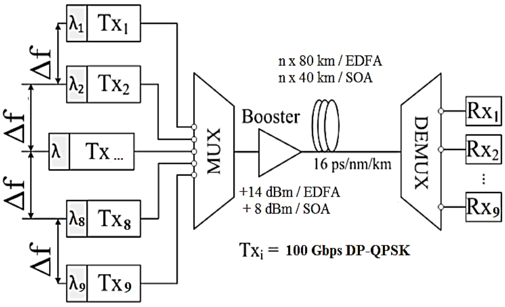

Fig. 1. Simplified DWDM system design for Q factor evaluation.

Transmitter model is displayed in Fig. 2.

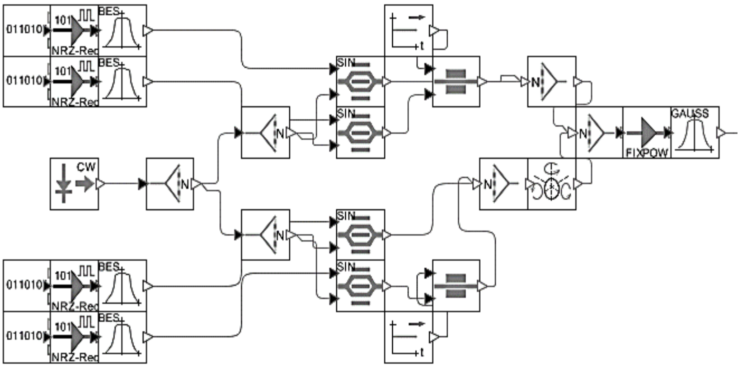

Fig. 2. 100 Gbps DP-QPSK transmitter model.

The central wavelength was set for 193.0 THz, instead of standard 193.1, in order to consider possible additional disturbances, e.g., higher fibre losses [16]. The continuous wave (CW) laser source was divided into four constant 0 dBm beams, each was managed by 25 Gbps pseudo-random bit generators through electrical pulse generators and amplitude modulators. Further, 90° phase modulation was performed on two modulated optical beams and after phase modulation two signals with orthogonal phases were combined for further polarization modulation. All four optical signals were combined and transmitted through the two-sided optical Gaussian filter; – 3 dB bandwidth equals to 35 GHz.

The rationale for channel number was defined by the non-linear distortion statistical calculation [17], which showed that the impact of the non-linear cross-phase modulation (XPM) on specific transmission channel reached ~97 % of its maximum from four subsequent channels at both sides of the spectral band. The generated and combined optical signals are then amplified either by EDFA amplifier model with fixed output power of 14 dBm and NF = 4.5, or by SOA model with 8 dBm signal gain, *NF* = 8 and 14 dBm typical saturation power (P_{sat}).

From [12], it should be noted that SOA performance can have two regimes – static, assuming no gain fluctuations, and dynamic. Static regime can be found as follows (1):

$$h(t) = ln(G_0) - \left[\frac{P_{in}(t)}{P_{sat}}\right] * \left[e^{h(t)} - 1\right] , \quad (1)$$

where $h(t)$ is the SOA gain exponent, G_0 is the SOA small signal gain and $P_{in}(t)$ is the SOA input power.

From (1), we can extract two different cases – linear, when P_{in} « P_{sat} and non-linear, when the $P_{in}(t)$ approaches the saturation power P_{sat} of SOA, which decreases the level of static gain. The degradation examples of SOA static gain exponent caused by nonlinear distortions are depicted in Fig. 3 by solving SOA gain equation using the 4th order Runge Kutta method. Two SOA saturation powers were considered to illustrate different impact degrees [12].

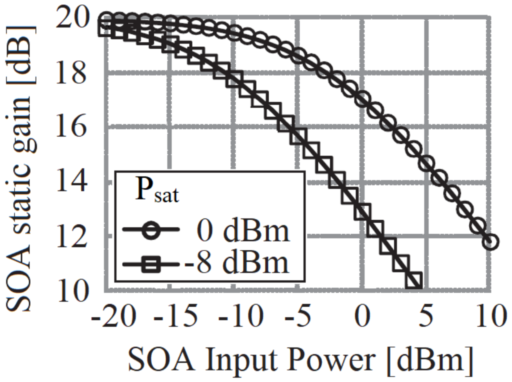

Fig. 3. SOA gain reduction caused by input power.

Dynamic regime, in its turn, presumes the $P_{in}(t)$ and $h(t)$ oscillate around their medians P_{in_av} (2) and h_{av} (3):

$$P_{in}(t) = P_{in\_av} + \Delta P_{in}(t); \quad (2)$$

$$h(t) = h_{av} + \Delta h(t). \quad (3)$$

In the dynamic regime the SOA gain, considering few approximations [12], can be expressed as follows (4):

$$\left[1+\tau_c * \frac{d}{dt}\right] * \Delta h(t) = -\left[\frac{\Delta P_{in}(t)}{P_{sat}}\right] * e^{h_{av}}, \quad (4)$$

where τ_c refers to carrier lifetime. From Eq. (4), it can be concluded that the dynamic SOA gain (gain fluctuation) does not take place in the linear regime ($P_{in}(t) \ll P_{sat}$). Nevertheless, it should be noted that in the non-linear state the gain fluctuations are affected by the signal envelope oscillations in the SOA input. This raises additional considerations and points to the sensitivity of the SOA nonlinearities to modulation formats using time-varying power envelopes [12] and provides the rationale for signal modulation choice in this research. As an example, to depict correlation between input and saturation power relation and Q level, it can be calculated that if the input power takes two values of 0 dBm and 5 dBm with 6 dBm saturation power, the Q^2 level reaches 12 dB and 5 dB, respectively ($\Delta Q^2 = 7$ dB). It should be mentioned that SOAs with the higher saturation power are less exposed to the adverse non-linear distortions [12].

The above-mentioned relations determined the 40 km optical fibre span (*Ls*) for SOA system, since the operation around 14–16 dBm power for higher fibre span losses could adversely impact the spectral shape of amplification curve and, as a result, overall system performance. This scenario needs to be studied in more detail separately in future research.

Further, the amplified signal was launched into the optical fibre (using 40 km span for SOA systems and 80 km for EDFA systems), where loss $\alpha = 0.2$ dB/km, effective area = 80 µm2, the dispersion coefficient $D = 16$ ps/nm/km, and the Kerr nonlinear coefficient $\gamma = 1.26$ 1/W/km. Guided by the recent studies which evaluated signal transmission quality by considering different SOA parameters and WDM transmission system configurations [12], [13], it was decided to compensate accumulated dispersion after an opto-electric conversion by the electronic dispersion compensation (EDC) module at a receiver side instead of optical fibre dispersion compensation module (DCM) incorporated directly after the transmission fibre link.

At a receiver side, each signal was filtered from a common optical flow by two-sided Gaussian filter; -3 dB bandwidth was carefully tuned for each transmission length in order to define bandwidth value granting the highest transmission quality. Such evaluation example for SOA system with *Lp* = 80 km is depicted in Fig. 4.

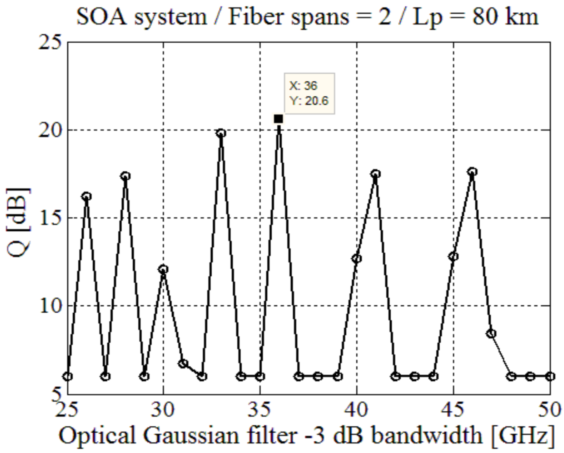

Fig. 4. Optical Gaussian filter tuning.

Further, 100 Gbps DP-QPSK signal was divided into four 25 Gbps signals by 4 by 4 QPSK split combiner, based on their phase and polarization and then converted by PIN photodetectors into electrical signals, passed through Bessel filter, EDC and detected by Q estimator and electrical scope. Receiver block diagram is shown in Fig. 5.

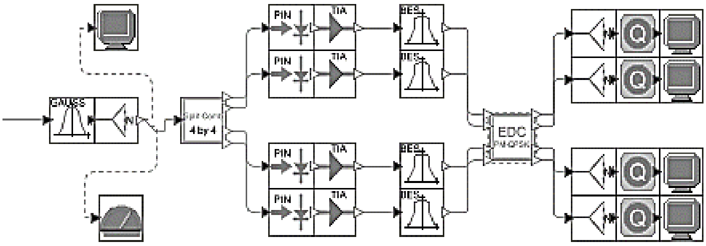

Fig. 5. 100 Gbps DP-QPSK receiver model.

The transmission length was simulated by using an iteration loop feature and specifying a number of fibre spans (*Nsp*) for EDFA and SOA amplification systems. In this study, we simulated 5 transmission lengths – 80 km, 160 km, 240 km, 320 km and 640 km and for each we found a set of parameters to fulfil Q level requirement >16 dB using standard channel spacing $\Delta f = 50$ GHz. It strengthened the assumption that SOAs could be used as alternative amplification devices instead of EDFAs, maintaining the same frequency grid, which in its turn could make strategic implementation more feasible.

3. RESULTS AND DISCUSSION

During the next step, the analytical model was designed within Matlab environment. Considering channel granularity Δf=50 GHz, the utilized bandwidths were defined separately for EDFA, which was standard C-band (1530–1565 nm) with 86 channels (N_{ch_edfa}), and for SOA amplification systems – 1530–1605 nm, excluding wavelengths from 1565 nm to 1569 nm due to a lack of available laser sources in the transition interval between C and L bands [12], having 182 transmission channels in total amplified by SOAs (N_{ch_soa}). Such allocation resulted in ≈ 2.12 times greater transmission capacity (18.2 TBit/s) and 7 % higher spectral efficiency compared to EDFA (*SE* = 2.10 and 1.96 bit/Hz, respectively).

Further, the power consumption levels were defined based on available component datasheets: for DP-QPSK transceivers P_{tx} = 19 W, SOA P_{soa_amp} = 4 W and EDFA power consumption P_{edfa_amp} = 30 W. Now the power efficiency values can be calculated and compared (5) (Figs. 6 and 7).

$$PE_x = P_x / BW_x, \tag{5}$$

where X refers to specific parameter of either EDFA or SOA system, PE_x – power efficiency [W/Hz], BW_x – utilised spectral bandwidth [Hz], P_x – total power consumption [W].

$$P_x = N_{ch\_x} * P_x + N_{sp} * P_{x\_amp}. \tag{6}$$

Unlike results of the previous studies [14], [15], [18], power consumption of ROADM terminals was not included in total power consumption calculations, focusing on system components that required defining the amount of used power and emphasising signal generation and regeneration power needs.

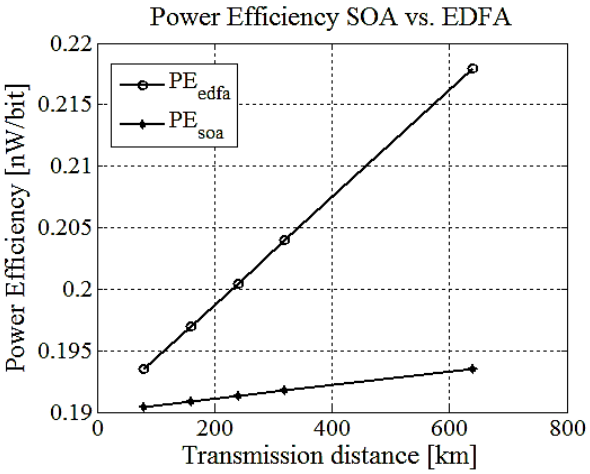

Fig. 6. Power efficiency levels at the considered transmission distances.

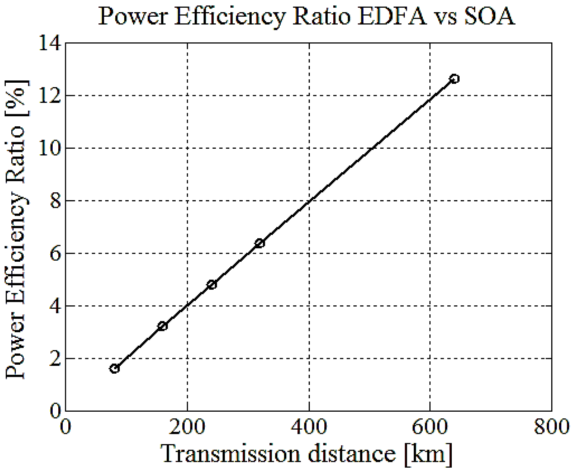

Fig. 7. Relation of power efficiency levels for EDFA and SOA amplification systems.

4. CONCLUSION

Motivated by a growing number of studies focused on SOA performance evaluations as an alternative low-cost amplification component for DWDM systems, the main aim of this study was to evaluate the impact on the power efficiency levels substituting EDFAs with SOAs, considering recent findings regarding SOA capabilities and relevant analytical methods. To reach this aim, in the current research we evaluated and compared the power efficiency levels in the proposed substitution scenario, when total capacity of EDFA-amplified optical link, which utilised 86 channels in C-Band, was doubled by usage of SOAs instead, providing 182 transmission channels due to wider amplification band. In both configurations, 100 Gbps DP-QPSK transmission signals separated by 50 GHz channel spacing were used.

During the first simulation step, it was shown that considering correlation between non-linear distortions and ratio of semiconductor amplifier input power $P_{in}(t)$ and saturation power P_{sat}, it was possible to adjust transmission parameters in such a way to guarantee Q factor at the receiving node greater than 16 dB over 640 km fibre link.

Further, based on the obtained results and available transmission system component parameters, the power efficiency levels were calculated. The comparison of calculated values showed that the system with SOA amplification required less energy for a single bit transmission and that difference became more considerable for greater transmission distances – from 1.6 % to 12.6 %, for 80 km and 640 km, respectively, proving that SOAs along with relatively low component costs, could grant additional ecological and financial benefits.

It should be noted that, since this is the first step to assess energy consumption volumes for SOA amplified systems, several potentially critical system parameters, physical impairments and hardware availability and compatibility questions are out of the scope of this research and must be analysed in future studies.

REFERENCES

1. Cisco Systems, Inc. (2020). *Cisco Annual Internet Report (2018–2023)*. Available at https://www.cisco.com/c/en/us/solutions/collateral/executive-perspectives/annual-internet-report/white-paper-c11-741490.html
2. Ghazisaeidi, A., de Jauregui Ruiz, I.F., Rios-Muller, R., Schmalen, L., Tran, P., Brindel, P., …& Renaudier, J. (2016). 65Tb/s transoceanic transmission using probabilistically shaped PDM-64QAM. In: *42nd European Conference on Optical Communication*, 18–22 September 2016, Dusseldorf, Germany.
3. Cai, J.-X., Batshon, H.G., Mazurczyk, M.V., Sinkin, O.V., Wang, D., Paskov, M., … & Foursa, D.G. (2018). 51.5 Tb/s Capacity over 17,107 km in C+L Bandwidth Using Single-Mode Fibres and Nonlinearity Compensation. *Journal of Lightwave Technology, 36* (11), 2135–2141. DOI: 10.1109/JLT.2018.2802322
4. Zhang, S., Yaman, F., Huang, Y.-K., Downie, J.D., Zou, D., Wood, W.A., … & Inada, Y. (2016). Capacity-approaching transmission over 6375 km at spectral efficiency of 8.3 bit/s/Hz. In: *2016 Optical Fibre Communications Conference and Exhibition (OFC)*, 20–24 March 2016, Anaheim, CA, USA.
5. Malmodin, J., & Lundén, D. (2018). *The Energy and Carbon Footprint of the Global ICT and E&M Sectors 2010–2015, Sustainability*. Available at https://www.researchgate.net/publication/327248403_The_Energy_and_Carbon_Footprint_of_the_Global_ICT_and_EM_Sectors_2010-2015
6. Essiambre, R., Kramer, G., Winzer, P.J., Foschini, G.J., & Goebel, B. (2010). Capacity Limits of Optical Fibre Networks. *Journal of Lightwave Technology*, *28* (4), 662–701. DOI: 10.1109/JLT.2009.2039464

7. Ghazisaeidi, A., de Jauregui Ruiz, I.F., Rios-Muller, R., Schmalen, L., Tran, P., Brindel, P., … & Renaudier, J. (2017). Advanced C+L-Band Transoceanic Transmission Systems Based on Probabilistically Shaped PDM-64QAM, *Journal of Lightwave Technology*, *35* (7), 1291–1299. DOI: 10.1109/JLT.2017.2657329
8. Ionescu, M., Lavery, D., Edwards, A., Sillekens, E., Galdino, L., Semrau, D., … & Bayvel, P. (2019). 74.38 Tb/s transmission over 6300 km single mode fibre with hybrid EDFA/Raman amplifiers. In: *Optical Fibre Communications Conference and Exhibition (OFC)*, (pp. 1–3), 3–7 March 2019, San Diego, California, USA. Available at https://arxiv.org/abs/1902.09821
9. Akiyama, T., Ekawa, M., Sugawara, M., Sudo, H., Kawaguchi, K., Kuramata, A., … & Arakawa, Y. (2004). An ultrawide-band (120 nm) semiconductor optical amplifier having an extremely-high penalty-free output power of 23 dBm realized with quantum-dot active layersb. In: *Optical Fibre Communication Conference,* 22 February 2004, Los Angeles, California, USA.
10. Renaudier, J., Meseguer, A.C., Ghazisaeidi, A., Tran, P., Rios-Muller, R., Brenot, R., … & Charlet, G. (2017). First 100-nm continuous-band WDM transmission system with 115Tb/s transport over 100km using novel ultra-wideband semiconductor optical amplifiers. In: *2017 European Conference on Optical Communication (ECOC)*, (pp. 1–3), 17–21 September 2017, Gothenburg: IEEE. DOI: 10.1109/ECOC.2017.8346084
11. Renaudier, J., Meseguer, A.C., Ghazisaeidi, A., Brindel, P., Tran, P., Verdier, A., … & Charlet, G. (2018). Field trial of 100nm ultra-wideband optical transport with 42GBd 16QAM real-time and 64GBd PCS64QAM channels. In *2018 European Conference on Optical Communication (ECOC)*, (pp. 1–3), 23–27 September 2018, Rome, Italy: IEEE. DOI: 10.1109/ECOC.2018.8535349
12. Bendimerad, D.F., & Frignac, Y. (2017). Numerical Investigation of SOA Nonlinear Impairments for Coherent Transmission Systems Based on SOA Amplification. *Journal of Lightwave Technology*, *35* (24), 5286–5295. DOI: 10.1109/JLT.2017.2772223
13. Ghazisaeidi, A. (2019). Theory of Coherent WDM Systems Using In-line Semiconductor Optical Amplifiers. *J. Lightwave Technol.*, *37*, 4188–4200. DOI: 10.1109/JLT.2019.2921864
14. Pavlovs, D., Bobrovs, V., Vilcāne, K., & Ivanovs, G. (2019). Investigation of optical signal regeneration impact on power efficiency of single-line-rate and mixed-line-rate wavelength division multiplexing systems. In: *PhotonIcs & Electromagnetics Research Symposium – Spring (PIERS-Spring)*, (pp. 896–901), 17–20 June 2019, Rome, Italy: IEEE. DOI: 10.1109/PIERS-Spring46901.2019.9017644
15. Pavlovs, D., Bobrovs, V., Parfjonovs, M., Alsevska, A., & Ivanovs, G. (2017). Evaluation of Signal Regeneration Impact on the Power Efficiency of Long-Haul DWDM Systems. *Latvian Journal of Physics and Technical Sciences*, *54* (5), 68–77. DOI: 10.1515/lpts-2017-0035
16. Agrawal, G.P. (2007). *Nonlinear Fibre Optics*. New York, NY, USA: Academic.
17. Velasco, L., Jirattigalachote, A., Ruiz, M., Monti, P., Wosinska, L., & Junyent, G. (2012). Statistical approach for fast impairment-aware provisioning in dynamic all-optical networks. *IEEE/OSA Journal of Optical Communications and Networking, 4* (2), 130–141. DOI: 10.1364/JOCN.4.000130
18. Pavlovs, D., Parts, R., Muratbeck, D., & Bobrovs, V. (2017). Comparison of power efficiency and signal regeneration impact in the SLR DWDM transmission systems with different spectral band. In: *Progress in Electromagnetics Research Symposium – Fall (PIERS - FALL)*, (pp. 1122–1127), 19–22 November 2017. Singapore: IEEE.

LATVIAN JOURNAL OF PHYSICS
AND TECHNICAL SCIENCES
2022, N 1

DOI: 10.2478/lpts-2022-0006

THE LEAST-COST OPTIMIZATION OF PV-STATION DC/AC EQUIPMENT USING BATTERY ENERGY STORAGE SYSTEM

I. Buratynskyi*, T. Nechaieva

Institute of General Energy of the National Academy of Sciences of Ukraine,
172 Antonovycha Str., Kyiv, 03150, UKRAINE
*e-mail: buratunsky@gmail.com

The auction allocation of state support quotas for renewable generation implementation that will change the existing incentive for their development by providing "green" tariffs to producers is based on competitive selection of the power plant projects with the least cost of electricity generation. The competitive advantage of solar photovoltaic power plant (PV stations) projects can be done by deciding what kind of equipment can provide the minimum cost of electricity generation during the period of operation. In the article, there is improvement of non-linear mathematical least-cost optimization model of the structure of PV-station equipment using DC coupled battery energy storage system (BESS) to store the excess electricity of photovoltaic modules (PV modules), which is lost on inverters when they are overloaded during the hours of the highest intensity of solar radiation. The article presents the modelling results of overall operation of PV station with fixed power of PV modules, as well as determines optimal power of inverter equipment and battery capacity. The model calculations have shown that when the DC equipment costs of the PV station are reduced by almost 62 % and DC equipment costs of BESS are reduced by 86.7 % of the actual value in 2020 at the power of 10 MW PV modules, the optimal power of inverter equipment decreases from 7.08 to 6.29 MW, and the storage capacity increases from 0.22 to 2.51 MWh. The use of BESS allows accumulating the amount of electricity produced by PV modules, which is lost with limitation on inverters, while the cost of their joint electricity production is decreased by 0.42 %.

Keywords: *BESS, DC/AC overloading, levelized daily cost of electricity, nonlinear modelling, optimization, PV station.*

1. INTRODUCTION

In recent years, in Ukraine and in the world there is a sharp increase in the installed capacities of renewable energy source (RES) generation. It is related to the fact that the countries of the world are willing to promote sustainable development with the transition to the "green" clean energy in order to achieve global climate goals of the Paris Agreement. According to the target indicators of the Energy Strategy of Ukraine [1], the development of generating capacities in the period from 2020 to 2035 has to increase the share of RES in the total electricity production from 7 % to 25 %.

Among all the RES, PV stations have the highest rate of implementation. It is due to the rapid development of this sector, because the PV equipment and the design of power plants are improved on a regular basis. PV modules become more powerful and efficient every year and their cost falls sharply.

In Ukraine, the legislative incentive for implementation of RES generation by providing high "green" tariffs brought about a high increase in the installed capacity of PV stations. As of the end of 2020, their total power was 5.36 GW, which was 9.8 % of the total Integrated Power System (IPS) of Ukraine capacity; compared to 2019, it was 3.56 GW (6.7 %) and in 2018 – 1.22 GW (2.5 %) [2].

Along with such a rapid development, there is a number of problems related to further implementation of PV stations in Ukraine. Due to the specifics of PV stations to generate maximum power at noon and overall reduction of electricity consumption from the beginning of 2020 in IPS of Ukraine, the government is forced to introduce dispatch restrictions on power plants, including PV stations. This is due to insufficient flexibility of IPS of Ukraine with a significant share of baseload capacity.

High "green" tariffs for the RES producers, imperfect payments for electricity on the new electricity market have led to considerable debt and the need to take special measures in order to reduce these tariffs.

To overcome the non-payment crisis and to achieve the compliance of variable RES generation amount with the power system capabilities at the legislative level, new competitive conditions for auction allocation of quotas for their construction have been adopted since 2019. The main aim of capacity distribution is to reduce the cost of electricity generated by RES. The quotas will be distributed among those auction participants who will offer the lowest prices for the sale of electricity, which will be guaranteed to be paid to the producer.

Due to lower costs for implementation and maintenance of BESS to provide for more stable operation of power plants, their joint use with PV station is becoming more common.

The location of BESS at the site of the PV station as part of it has many advantages, because in this case there is no need to allocate a separate land plot and to obtain permits for construction. When BESS operates together with the PV station, there is no need to install additional equipment, because it is possible to share power transformers, electricity transmission lines and other equipment. In general, the total costs when installing BESS at the site of the PV station, as it is defined in the study related to cost indicators for the photovoltaic systems and the electricity storage systems [3], are 7–8 % lower than when they are located separately.

Based on the size of the land for the construction of the PV station, the investor, focusing on a certain DC power of PV modules, should select AC power of the inverter equipment that will provide the lowest cost of electricity generation, which will give the corresponding benefits when participating in the auction for the allocation of quotas for the new construction of the PV station.

At present, a particularly important task is to find the ways for minimization of PV station electricity production costs. One of the methods of reducing electricity production costs is to reduce AC power of inverter equipment at a fixed power of PV modules. As the results of the study [4] show, for the 10 MW PV station, located in the south of Ukraine, the lowest cost is achieved with DC/AC ratio of 1.4. At the same time, when the inverters are overloaded with excess power of PV modules, part of electricity that has to be output to power system is lost.

The aim of the study is to model an optimal least-cost structure of the PV station equipment using BESS in order to accumulate and output excess power of PV modules, which is lost with limitations on inverters.

2. THEORY

Nonlinear mathematical model of optimization of the PV station equipment structure [5] provides the choice of optimal AC power of inverter equipment with fixed DC power of PV modules to achieve the minimal cost of electricity generation during their lifetime depending on the intensity of solar radiation. The performed model calculations [5] showed the difference in the structure of PV station equipment for sunny and cloudy days at different levels of solar radiation. It means that the optimal structure of the PV station equipment is formed according to its geographical location, which is an important factor for the selection of equipment before the stage of participation in the auction for the allocation of quotas for installed capacity.

Further improvement of nonlinear mathematical model of optimising the PV station equipment structure was conducted to determine the structure of PV station equipment using BESS for storage and output of the excess power of PV modules with DC/AC overloading, which was lost on inverters, the joint operation of which would provide for the minimal cost of output electricity.

There are two main ways to connect BESS to PV station: AC coupled and DC coupled, each of them having its advantages and disadvantages. During construction of new power plants, it is better to use a DC coupled approach because in this case saving of generated and output electricity is from 1 to 4 % with joint operation of PV station and BESS as it is shown in the paper [6].

The joint operation of PV station and BESS means to connect batteries to the same busbars close to the central inverters together with PV modules. In this study, connection of BESS to PV station is done using a DC coupled approach. The simplified structure diagram is shown in Fig. 1.

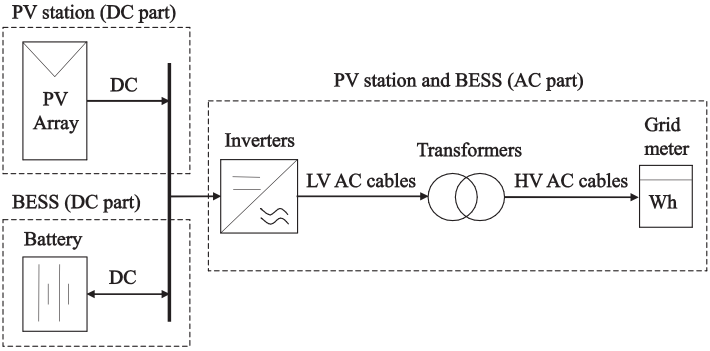

Fig. 1. The simplified structure diagram of PV station and BESS.

The objective function of the improved model is to minimise the levelized daily cost of electricity generation (LDCOE) with the joint operation of PV station and the use of BESS in the saving mode of losses of electric power of PV modules on inverters during their overloading. The total excess of PV module capacity, which is in excess of PV station inverter capacity, is accumulated in batteries with subsequent discharge during the day.

LDCOE is determined by the ratio of the capital investment costs during implementation and the summary of operational costs during the whole period of PV station and BESS operation lifetime, which are reduced to the weighted daily average and to daily volumes of output electricity during the joint operation of PV station and BESS taking into consideration the level of solar radiation.

$$LDCOE = \frac{P^{DC}(c^{DC}+o^{DC}) + P^{DC}x^{AC/DC}(c^{AC}+o^{AC}) + E^{BESS}/\eta^{RT}(c^{BESS}+o^{BESS})}{E^{PV}+E^{BESS}\eta^{RT}} \to \min, \qquad (1)$$

where $LDCOE$ is levelized daily cost of electricity when PV station and BESS operate together in the mode of saving electricity losses on inverters during their overloading, \$/MWh; P^{DC} is installed DC power of PV modules, MW; $x^{AC/DC}$ is variable AC/DC ratio (inverse coefficient to DC/AC ratio); c^{DC} is specific daily capital expenditure (CAPEX) for DC power, \$/MW; o^{DC} is specific daily operational expenditure (OPEX) for DC power, \$/MW; c^{AC} is specific daily CAPEX for AC power, \$/MW; o^{AC} is specific daily OPEX for AC power, \$/MW; E^{BESS} is excess electrical energy on inverters during overloading that accumulates in BESS, MWh; η^{RT} is round trip efficiency (RT) of BESS, share; c^{BESS} is specific daily CAPEX for BESS, \$/MWh; o^{BESS} is specific daily OPEX for BESS, \$/MWh; E^{PV} is generated electricity at the PV station and outputed into the power system, MWh.

The AC/DC variable ratio is determined as follows:

$$x^{AC/DC} = \frac{X^{AC}}{P^{DC}}, \qquad (2)$$

where X^{AC} is variable installed AC power of inverters, MW.

For the variable power ratio of alternating and direct current PV station in the model, the following restriction is set:

$$0.5 < x^{AC/DC} \le 1. \qquad (3)$$

The electrical energy output from the PV station to the power system is determined according to the intensity of solar radiation entering the PV-modules, taking into account the power limit of inverters [5]:

$$E^{PV} = \sum_{t=1}^{T} P^{PVout}{}_{t} \cdot \Delta t, \tag{4}$$

where T is the number of measurement intervals in one day (for hourly schedule $T = 24$); $P^{PVout}{}_{t}$ is the value of the generation power at the PV station, which is issued to the power system during the time *t* during the day, MW; Δt is the duration of one time period (hour).

The power supply of electricity from the PV station to the power system during time *t* is determined taking into account the limitation of inverter power depending on the level of solar radiation [5]:

$$P^{PVout}{}_{t} = \left[\begin{array}{l} P^{DC} x^{AC/DC}, \quad P^{DC} I_t \geq P^{DC} x^{AC/DC} \\ P^{DC} I_t, \quad P^{DC} I_t < P^{DC} x^{AC/DC} \end{array} \right. , \tag{5}$$

where I_t is intensity of solar radiation, relative units.

Excess electrical power on inverters during overloading is the BESS charging power. Therefore, the total accumulated electricity in BESS is defined as follows:

$$E^{BESS} = \sum_{t=1}^{T} P^{BESSchrg}{}_{t} \cdot \Delta t, \tag{6}$$

where $P^{BESSchrg}{}_{t}$ is the BESS charging power during time *t*, MW.

BESS charging power is determined as follows:

$$P^{BESSchrg}{}_{t} = \left[\begin{array}{l} P^{DC} I_t - P^{DC} x^{AC/DC}, \quad P^{DC} I_t \geq P^{DC} x^{AC/DC} \\ 0, \quad P^{DC} I_t < P^{DC} x^{AC/DC} \end{array} \right. . \tag{7}$$

OPEX of PV station and BESS during their joint work, equal to operating life for PV station, is reduced to annual levelized cost using a capital recovery factor (CRF). The total costs are considered to be evenly distributed for each day during the year.

Since the BESS is connected to the PV station on the DC side, there is no AC component of the inverter equipment in its CAPEX and OPEX costs.

The specific levelized daily capital investment costs for PV station equipment and BESS are determined as follows [5]:

$$c^{DC,AC,BESS} = (i^{DC,AC,BESS} + k^{DC,AC,BESS}) \cdot CRF / 365, \tag{8}$$

where $i^{DC,AC,BESS}$ is specific capital costs for PV station (\$/MW) and BESS (\$/MWh); $k^{DC,AC,BESS}$ is specific discounted interest payments on loans (\$/MW; \$/MWh); *CRF* is capital recovery factor; 365 is the number of days per year.

Specific capital costs for PV station and BESS are determined as follows [5]:

$$i^{DC,AC,BESS} = e^{DC,AC,BESS}(1+EPC^{DC,AC,BESS}), \tag{9}$$

where $e^{DC,AC,BESS}$ is specific costs on equipment (\$/MW; \$/MWh); $EPC^{DC,AC,BESS}$ is share of costs on engineering, procurement and construction (EPC) from CAPEX.

Specific discounted interest payments on loans are determined as follows [5]:

$$k^{DC,AC,BESS} = \sum_{t=T^{EPC}+1}^{m} \frac{c^K{}_t}{(1+r)^{t-T^{EPC}-1}}, \tag{10}$$

where $c^K{}_t$ is specific annual interest payments on loans attracted for investment (\$/MW; \$/MWh); T^{EPC} is years of EPC for PV station and BESS; m is a loan repayment period (years); r is a discount rate, %.

Specific levelized daily OPEX for DC and AC equipment of PV station and BESS is determined as follows:

$$o^{DC,AC,BESS} = \sum_{n=1}^{N} \frac{OM^{DC,AC,BESS}}{(1+r)^{n-1}} \cdot CRF/365. \tag{11}$$

where $OM^{DC,AC,BESS}$ is annual specific costs for operation and maintenance (O&M) for DC and AC equipment of PV station and BESS, \$/MWh; n is the current year of operation; N is the number of years of joint operation of PV station and BESS.

3. RESULTS AND DISCUSSION

10 MW DC power PV station, which is located close to the geographical centre of Ukraine in Cherkasy region, was chosen for the model calculations. The data on intensity of solar radiation were used from online resource PVGIS [7]. To study the territory, average data were received on intensity of solar radiation by the average value during the year.

Table 1 shows the technical and economic indicators used in the LDCOE calculations.

Table 1. Technical and Economic Data for Modelling

No	Indicator	Unit	Value
1	Discount rate	%	10.7
2	Share of investment costs covered by external loan	%	70
3	Interest rate	%	10.4
4	Loan repayment period	years	4
5	Installed DC power of PV modules	MW_{DC}	10
6	Operating lifetime of PV station and BESS	years	20
7	Construction period of PV station and BESS	years	1
8	Share of EPC costs of PV station equipment costs	%	14.0
9	Share of EPC costs of BESS equipment costs	%	11.2
10	Round trip efficiency of BESS	%	95.0

The CAPEX inputs for PV station given in the study about the future utility-scale PV LCOE until 2050 in several European countries [8] were used to conduct simulation. They are taken into account as costs of DC equipment. Input costs are converted from euro into dollars according to the exchange rate of 1.24. The specific cost of AC equipment is 215 $/kW with a similar trend going down in the coming years. OPEX inputs are taken from the study [8] with the breakdown in the percentage of costs for DC and AC equipment as 70 % and 30 %, respectively.

The data on CAPEX for DC equipment of BESS, the main component of which is batteries, are taken from Bloomberg NEF [9] and additional costs at the level of 9.5 % are taken into account to provide their normal functioning (HVAC, lighting, fire protection system, software, etc.). OPEX costs for DC equipment of BESS are taken as part of the costs at the level of 77 % from the study [8]. Other costs (23 %) are not taken into account because it is assumed that these are the costs for BESS AC equipment, which are absent in case of a DC coupled approach.

Table 2 shows the accepted input parameters and the obtained results of model calculations of the optimal DC/AC ratio of PV modules and inverter equipment PV station with BESS and without BESS.

Table 2. Input Data and Optimization Results

No	Indicator name	Unit	2020	2030	2040	2050
	Input data for PV station (DC part)					
1.1	Specific CAPEX	$/kW	534.0	341.0	253.0	203.0
1.2	Specific OPEX	$/kW/a	7.6	5.6	4.3	3.6
1.3	Specific daily CAPEX	$/kW	204.2	139.0	109.3	92.6
1.4	Specific daily OPEX	$/kW	60.3	47.1	40.6	36.9
	Input data for PV station (AC part)					
2.1	Specific CAPEX	$/kW	215.0	137.0	102.0	82.0
2.2	Specific OPEX	$/kW/a	3.3	2.4	1.9	1.6
2.3	Specific daily CAPEX	$/kW	82.1	55.9	44.0	37.2
2.4	Specific daily OPEX	$/kW	17.9	12.5	9.8	8.3
	Input data for BESS (DC part)					
3.1	Specific CAPEX	$/kWh	150.0	62.0	41.0	20.0
3.2	Specific OPEX	$/kWh/a	3.7	2.2	1.6	1.4
3.3	Specific daily CAPEX	$/kWh	56.23	23.24	15.37	7.5
3.4	Specific daily OPEX	$/kWh	19.19	10.04	7.06	5.2
	Results					
4.1	DC/AC ratio (PV station and BESS)	-	1.41	1.41	1.45	1.59
4.2	Inverter power (PV station and BESS)	MW	7.08	7.08	6.89	6.29
4.3	BESS capacity	MWh	0.22	0.22	0.62	2.51
4.4	Daily energy output of PV station	MWh	52.23	52.23	51.84	50.05
4.5	Daily energy output of PV station and BESS	MWh	52.42	52.42	52.40	52.31
4.6	PV station in total costs	%	20.23	13.21	11.79	7.37
4.7	BESS in total costs	%	79.77	86.79	88.21	92.63
4.8	LDCOE of PV station	$/MWh	64.21	44.90	35.99	30.96
4.9	LDCOE of PV station and BESS	$/MWh	64.28	44.87	35.94	30.83
4.10	Reduction LDCOE when using BESS	%	-0.11	0.07	0.14	0.42

The results of the model calculations show that when the prices for batteries go down the capacity of using BESS is increasing. When the specific costs of DC equipment for the PV station decrease almost by 62 % and the specific costs of DC equipment for BESS decrease by 86.7 % of the actual value of 2020, the capacity of storage increases from 0.22 to 2.51 MWh, and the optimized power of inverters reduces from 7.08 to 6.29 MW. The joint operation of the PV station and BESS in the mode of excess capacity of PV modules at the price of equipment as of 2050 provides minimum LDCOE, which is 0.42 % less than LDCOE in the operation of the PV station with losses when overloaded, and the additional use of 4.3 % of all the electricity supplied.

When batteries are cheaper, their use at the PV station in the mode of saving losses of excess electricity produced at the PV modules becomes increasingly cost effective. As an example to increase their profitability, it is better to send accumulated electricity from the batteries into the system when there is high demand and it is possible to sell it at a peak price.

Figure 2 shows an example of the daily schedule of the joint operation of the PV station and BESS when charging batteries during the period of maximum solar radiation according to the power limit of inverters taken into account in the optimization model. Discharge of batteries is done immediately after the end of the maximum of solar radiation according to the mathematical model of the joint operation of PV station and BESS [10], using the obtained optimization results at storage capacity of 2.51 MWh.

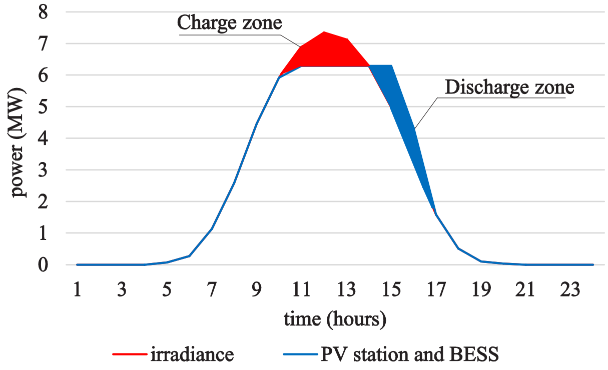

Fig. 2. The daily work schedule of joint PV station and BESS.

To save all the electricity produced by PV modules with limitations on inverters in the peak period of solar radiation, the zone of excess power of PV station is created (marked in red), which is a zone of charging batteries. The zone of battery discharge is created at once after lowering the maximum of solar radiation (marked in blue), taking into account losses during the reverse conversion of electrical energy.

4. CONCLUSIONS

Modern approaches to providing incentive for the development of RES by means of auction system of quota allocation for installed capacity change the approaches to implementation of new design for power plants. The main criterion of the auction system of quotas is to provide the electricity generation cost during the whole operational life at the lowest competitive level. Given the inexhaustible source of solar radiation for PV stations with no component of fuel consumption, it is possible to ensure minimum electricity production cost determining the optimal composition of its equipment in terms of the ratio of DC power of PV modules and AC power of inverter equipment.

Taking into consideration the fact that when overloaded the inverters cannot transmit all the generated electricity the restrictions are used for them. When limited, part of the generated electricity is lost. Although such measures reduce levelized cost, they also reduce the amount of electricity supplied. That is why the nonlinear mathematical model for optimization of the structure of PV station equipment is improved using BESS DC coupled to save the excess power of the PV modules when overloaded. During the joint operation of the PV station and BESS, all the electricity generated at the PV modules, which was previously lost on the inverters when they were overloaded, is stored in the batteries and then output to the power system is provided.

Introduction of BESS in the PV station influences the optimal structure of its equipment. When the battery prices are reduced, BESS capacity, which is needed to accumulate all the excess electricity on inverters, as a result of optimization is increased, and allows reducing the power of the PV station inverters.

As the results of modelling show, taking into account the changes of the dynamics of the specific costs until 2050, for PV stations with 10 MW PV modules the optimal power of inverters is reduced from 7.08 to 6.29 MW, and accumulation capacity increases from 0.22 to 2.51 MWh. The use of BESS allows saving around 4.3 % of the total daily electricity supply, which was lost preciously due to limitations on inverters. This way the levelized daily cost of electricity is reduced by 0.42 %.

REFERENCES

1. Ministry of Energy of Ukraine. (2017). *Energy Strategy of Ukraine for the Period up to 2035*. Available at http://mpe.kmu.gov.ua/minugol/control/uk/publish/article;jsessionid=B483C8B0C24F6D22E66D30CEB3198ED5.app1?art_id=245239564&cat_id=245239555
2. NPC “Ukrenergo”. (2020). *Installed Capacity of the IPS of Ukraine Values as of 12/2020*. Available at https://ua.energy/installed-capacity-of-the-ips-of-ukraine/#12-2020
3. Fu, R., Remo, T., & Margolis, R. (2018). *U.S. Utility-Scale Photovoltaics-Plus-Energy Storage System Costs Benchmark*. Golden, CO: National Renewable Energy Laboratory. NREL/TP-6A20-71714. Available at https://www.nrel.gov/docs/fy19osti/71714.pdf.
4. Buratynskyi, I., Nechaieva, T., & Shulzhenko, S. (2020). Optimization of the Equipment Structure of a Photovoltaic Solar Power Plant. *The Problems of General Energy, 2* (61), 17–22. https://doi.org/10.15407/pge2020.02.017
5. Bilenko, M., Buratynskyi, I., Leshchenko, I., Nechaieva, T., & Shulzhenko, S. (2021). Nonlinear Mathematical Model of Optimal Solar Photovoltaic Station Design. *Studies in Systems, Decision and Control*, *346*, 49–61. https://doi.org/10.1007/978-3-030-69189-9_3

6. Walsh, D., Bradshaw, D., Clamp A., & Russell K. (2020). Optimizing Solar PV Plus Battery Storage. *Business & Technology Surveillance*. National Rural Electric Cooperative Association (NRECA).
7. Photovoltaic Geographical Information System. (PVGIS). (n.d.). Available at https://ec.europa.eu/jrc/en/pvgis
8. Vartiainen, E., Masson, G., Breyer, C., Moser, D., & Román Medina E. (2019). Impact of Weighted Average Cost of Capital, Capital Expenditure, and Other Parameters on Future Utility-Scale PV Levelised Cost of Electricity. *Prog Photovolt Res Appl, 28*, 439–453. https://doi.org/10.1002/pip.3189
9. BloombergNEF. (2020). *Battery Pack Prices Cited Below $100/kWh for the First Time in 2020, While Market Average Sits at $137/kWh*. Available at https://about.bnef.com/blog/battery-pack-prices-cited-below-100-kwh-for-the-first-time-in-2020-while-market-average-sits-at-137-kwh/
10. Buratynskyi, I., & Nechaieva, T. (2020). Modeling of the Combined Operation of a Solar Photovoltaic Power Plant and a System of Electric Energy Storage. *The Problems of General Energy, 3* (62), 30–36. https://doi.org/10.15407/pge2020.03.030